Supporting Information to accompany

Understanding the Origin of One- or Two-Step Valence Tautomeric Transitions in Bis(dioxolene)-Bridged Dinuclear Cobalt Complexes

Gemma K. Gransbury, Brooke N. Livesay, Jett T. Janetzki, Moya A. Hay, Robert W. Gable, Matthew P. Shores, Alyona Starikova, Colette Boskovic

Table of Contents

Experimental and Synthetic Methods

Synthesis. *Materials and Methods.* All chemicals were of reagent grade and used as received. Where dry solvent is specified, it was dried over 3 Å molecular sieves for three days (acetonitrile) or one week (methanol). Where degassed solvent is specified, it was degassed by a minimum of five cycles of vigorous shaking under vacuum and back-filling with nitrogen. *Caution!* Perchlorate salts of organic materials or metal complexes are potentially explosive and should not be heated when dry. Handle in small quantities with sufficient care.[1]

Ligand synthesis. The precursor 6-formaldoximo-2-methylpyridine was synthesized from 6-methyl-2-pyridine carboxaldehyde according to the literature procedure and the resulting solid was dried in the presence of phosphorous pentoxide.[2] The ligand precursor 6-methyl-2-aminomethylpyridine was synthesized using a modified literature procedure.[2] To maximize yield the hydrogenation was undertaken on a diluted (not saturated) solution of 6-formaldoximo-2-methylpyridine in dry methanol with 10 wt.% Pd/C. The reaction mixture was contained a glass vessel and stirred overnight in a Buchi miniclave steel reactor under a hydrogen pressure of 280 psi. The yellow oil obtained after hydrogenation analyzed as 85–96% 6-methyl-2-aminomethylpyridine by NMR and was used without further purification. Ligands $(H_3tpa)(ClO_4)_3$, Me_2tpa and Me_3tpa were synthesized based on a modified literature procedure.[3] The tpa ligand was extracted with hot cyclohexane and isolated as the perchlorate salt by addition of perchloric acid. The Me_2tpa ligand was purified by recrystallization from heptane. The Me_3tpa ligand was isolated from the organic residue by recrystallization from hexane then diethyl ether. The free tpa ligand was alternatively synthesized via bis(2-pyridylmethyl)amine based on the literature procedure,[4] which is given below. The proligand $Br_4spiroH_4$ was synthesized based on a literature

procedure[5] with purification by recrystallization from hexane/diethyl ether, which gave rise to single crystals of diffraction quality. Both Br_4spiroH_4 and spiroH_4 were used as racemic mixtures.

Bis(2-pyridylmethyl)amine. Freshly distilled 2-pyridinecarboxaldehyde (4.76 mL, 50.0 mmol) and freshly distilled 2-aminomethylpyridine (5.15 mL; 50.0 mmol) were dissolved in dry, degassed methanol (65 mL). The reaction was stirred for 2 h at room temperature, then cooled to –62 °C for the addition of sodium borohydride (1.89 g, 50.0 mmol) in small portions. The temperature was maintained at –62 °C until the sodium borohydride dissolved. The reaction was then allowed to warm to room temperature and was stirred for 15 h. A saturated aqueous solution of ammonium chloride (150 mL) was added gradually and the reaction mixture was stirred until no bubbles were formed. The methanol was removed under reduced pressure and the remaining aqueous phase extracted with dichloromethane (3 × 100 mL). Combined organic extracts were dried over magnesium sulfate and allowed to evaporate overnight. The product was extracted from the organic residue with minimum isopropanol which was then removed under reduced pressure to give bis(2-pyridylmethyl)amine as a yellow oil, yield (85–90%) and characterization as previously reported.[4] ^{1}H NMR (400 MHz, $CDCl_3$, δ): 8.57 (d, J = 4.8 Hz, 2H, Ar-H), 7.67 (td, J = 7.6, 1.8 Hz, 2H, Ar-H), 7.37 (d, J = 7.6 Hz, 2H, Ar-H), 7.20 (dd, J = 7.6, 4.8 Hz, 2H, Ar-H), 4.08 (s, 4H, CH_2).

Tris(2-pyridylmethyl)amine (tpa). Potassium carbonate (4.15 g, 30.0 mmol) was added to a solution of bis(2-pyridylmethyl)amine (2.00 g, 10.0 mmol) in dry, degassed acetonitrile (10 mL). The reaction mixture was wrapped in aluminum foil to exclude light and 2-chloromethylpyridine (1.97 g, 12.0 mmol) was added in small portions. The reaction mixture was sealed under nitrogen and stirred for 6 days. The reaction was filtered, and the filtrate was evaporated overnight. The product was extracted from the organic residue with many portions of hot hexane (7 × 100 mL).

The white solid obtained upon evaporation was recrystallized from hexane and dried under reduced pressure to give tris(2-pyridylmethyl)amine as white crystals (2.96 g, 43%). Previously reported: 63%.[4] ^{1}H NMR (400 MHz, dmso-d_6, δ) 8.49 (ddd, J = 4.8, 1.8, 0.9 Hz, 3H, Ar-H), 7.77 (td, J = 7.7, 1.8 Hz, 3H, Ar-H), 7.59 (m, 3H, Ar-H), 7.25 (ddd, J = 7.7, 4.8, 1.1 Hz, 3H, Ar-H), 3.77 (s, 6H, CH_2).

[{Co(Me$_2$tpa)}$_2$(spiro)](PF$_6$)$_2$ (**1a**). A degassed methanolic (10 mL) solution of spiroH_4 (55.8 mg, 0.164 mmol) deprotonated with triethylamine (91.4 μL, 0.656 mmol) was added to a degassed methanolic (15 mL) solution of $CoCl_2 \cdot 6H_2O$ (76.6 mg, 0.322 mmol) and Me_2tpa (0.103 g, 0.324 mmol) under a nitrogen atmosphere. The solution was concentrated under reduced pressure and stirred under nitrogen for 10 mins. The red-orange solution was bubbled with a stream of compressed air and immediately turned black. The product was precipitated from solution by dropwise addition of a saturated aqueous potassium hexafluorophosphate solution. The crude solid was collected by vacuum filtration, washed with ethanol (2 × 1 mL) and diethyl ether (3 × 2 mL) and allowed to air dry to give a gray-green solid. The product was recrystallized twice by layering dichloromethane with diethyl ether in an inert atmosphere to give **1a**$\cdot CH_2Cl_2$ as a dark black-green microcrystalline solid (0.145 g, 61%). Anal. Calcd for $C_{62}H_{66}N_8O_4Co_2P_2F_{12}Cl_2$: C, 50.80; H, 4.54; N, 7.64. Found: C, 51.28; H, 4.18; N, 7.62. HRMS (ESI-QTOF) *m/z*: M^{2+} calcd for $C_{61}H_{64}N_8O_4Co_2$, 545.1857; found, 545.1864. TGA data is consistent with the presence of solvent. IR (KBr) $\bar{\nu}_{max}$: 1610 (m), 1578 (w), 1480 (s), 1454 (m), 1445 (sh), 1412 (w), 1287 (m), 843 (vs), 557 (s) cm^{-1}. UV/vis (acetonitrile) λ_{max} (ε): 369 (4480sh), 401 (3500), 421 (3010sh), 550 (1880sh), 576 (1980), 652 nm (1420sh mol L^{-1} cm^{-1}).

[{Co(tpa)}$_2$(Br$_4$spiro)](PF$_6$)$_2$ (**2a**). Degassed methanolic solutions of tpa (0.141 g, 0.487 mmol; 30 mL) and Br$_4$spiroH_4 (0.145 g, 0.221 mmol; 20 mL) deprotonated with triethylamine

(0.124 mL, 0.890 mmol) were sequentially added to a degassed methanolic solution of $CoCl_2 \cdot 6H_2O$ (0.105 g, 0.442 mmol; 10 mL) under a nitrogen atmosphere. The deep red solution was bubbled with a stream of compressed air for 1 h until it became dark green. The product was precipitated from solution by dropwise addition of a saturated aqueous potassium hexafluorophosphate solution (approx. 5 mL). The crude solid was collected by vacuum filtration, washed with 5:1 methanol/water (1 × 2 mL), ethanol (2 × 5 mL) and diethyl ether (4 × 5 mL) and allowed to air dry to give a green solid (0.259 g, 71%). The product was recrystallized by slowly cooling a hot methanolic solution to give **2a**·$4H_2O$ as a green microcrystalline solid. Single crystals suitable for X-ray diffraction were obtained by slowly cooling a methanolic solution. Anal. Calcd for $C_{57}H_{60}N_8O_8Br_4Co_2P_2F_{12}$: C, 39.98; H, 3.53; N, 6.54. Found: C, 39.97; H, 3.80; N, 6.47. HRMS (ESI-QTOF) *m/z*: M^{2+} calcd for $C_{57}H_{52}N_8O_4Br_4Co_2$, 674.9739; found, 674.9652. TGA data are consistent with four water molecules per complex. IR (KBr) $\bar{\nu}_{max}$: 1610 (m), 1576 (w), 1430 (vs), 1329 (m), 1268 (s), 1233 (w), 844 (vs), 558 (s) cm^{-1}. UV/vis (acetonitrile) λ_{max} (ε): 473 (353sh), 674 nm (516 mol L^{-1} cm^{-1}).

[{Co(tpa)}$_2$(Br$_4$spiro)](ClO$_4$)$_2$ (**2b**). A methanolic solution (5 mL) of $(H_3tpa)(ClO_4)_3$ (0.794 g, 1.34 mmol) was deprotonated with triethylamine (0.40 mL, 2.9 mmol) and added to a methanolic solution (5 mL) of $Co(ClO_4)_2 \cdot 6H_2O$ (0.500 g, 1.37 mmol). After 10 min of stirring at room temperature, a methanolic solution (5 mL) of $Br_4spiroH_4$ (0.433 g, 0.660 mmol) deprotonated with triethylamine (0.20 mL, 1.4 mmol), was added dropwise. The reaction mixture was refluxed for 2 h, then cooled to room temperature. The precipitate was collected by vacuum filtration, washed with methanol (2 × 5 mL) and diethyl ether (2 × 5 mL) and air dried to give crude **2b** as a green solid (0.450 g, 44%). Single crystals suitable for X-ray diffraction were obtained by vapor diffusion of an acetone solution with hexane or cyclohexane to obtain either diamond-shaped

plates (*pp*-[{Co(tpa)}$_2$(Br$_4$spiro)](ClO$_4$)$_2$·7acetone, **2b$_{pp}$**·7acetone) or hexagonal rods (*pd*-[{Co(tpa)}$_2$(Br$_4$spiro)](ClO$_4$)$_2$·3.9acetone, **2b$_{pd}$**·3.9acetone). Single crystals were unstable to evaporation of the mother liquor, appearing hygroscopic, and were immediately mounted on the diffractometer. The crude product was recrystallized by vapor diffusion of acetone with hexane and appeared hygroscopic, analyzing as **2b**·3H$_2$O. Anal. Calcd for $C_{57}H_{58}N_8O_{15}Br_4Co_2Cl_2$: C, 42.69; H, 3.65; N, 6.99. Found: C, 42.42; H, 3.58; N, 6.90. HRMS (ESI-QTOF) *m/z*: M^{2+} calcd for $C_{57}H_{52}N_8O_4Br_4Co_2$, 674.9739; found, 674.9722. TGA data show the onset of desolvation at 25 °C and are consistent with 3 water solvate per molecule, lost over one broad step centered at 47 °C. IR (KBr) $\bar{\nu}_{max}$: 1610 (m), 1574 (w), 1430 (vs), 1440 (sh), 1330 (m), 1267 (s), 1233 (w), 1090 (s), 627 (m) cm^{-1}. UV/vis (acetonitrile) λ_{max} (ε): 473 (375sh), 674 nm (496 mol L^{-1} cm^{-1}).

[{Co(Me$_2$tpa)}$_2$(Br$_4$spiro)](PF$_6$)$_2$ (**3a**). A degassed methanolic (30 mL) solution of Br$_4$spiroH$_4$ (0.246 g, 0.375 mmol) was deprotonated with triethylamine (0.209 mL, 1.50 mmol) and added to a degassed methanolic (15 mL) solution of CoCl$_2$·6H$_2$O (0.179 g, 0.750 mmol) and Me$_2$tpa (0.241 g, 0.756 mmol) under a nitrogen atmosphere. The dark red solution was bubbled with a stream of compressed air for 30 min until it became dark brown. The product was precipitated from solution by dropwise addition of a saturated aqueous potassium hexafluorophosphate solution. The crude solid was collected by vacuum filtration, washed with water (2 × 5 mL), isopropanol (2 × 5 mL), ethanol (2 × 5 mL) and diethyl ether (2 × 5 mL) and allowed to air dry to give a tan colored solid (0.548 g, 86%). The product was recrystallized by layering a dichloromethane solution with diethyl ether to give **3a** as a tan colored microcrystalline solid. Single crystals suitable for X-ray diffraction were obtained by layering a dichloromethane solution with 1,4-dioxane, *pp*-[{Co(Me$_2$tpa)}$_2$(Br$_4$spiro)](PF$_6$)$_2$·4.5dioxane (**3a**·4.5dioxane). Anal. Calcd for $C_{61}H_{60}N_8O_4Co_2Br_4P_2F_{12}$: C, 43.18; H, 3.56; N, 6.60. Found: C, 42.99; H, 3.94; N, 6.49.

HRMS (ESI-QTOF) *m/z*: M^{2+} calcd for $C_{61}H_{60}N_8O_4Br_4Co_2$, 703.0053; found, 703.0098. IR (KBr) $\bar{\nu}_{max}$: 1612 (m), 1577 (w), 1443 (s), 1329 (w), 1273 (s), 1237 (w), 845 (vs), 557 (s) cm^{-1}. UV/vis (acetonitrile) λ_{max} (ε): 388 (1770sh), 535 (397sh), 809 nm (515 mol L^{-1} cm^{-1}).

[{Co(Me$_3$tpa)}$_2$(Br$_4$spiro)](PF$_6$)$_2$ (**4a**). Compound **4a** was prepared as per **3a** from $Br_4spiroH_4$ (0.248 g, 0.378 mmol), triethylamine (0.211 mL, 1.51 mmol), $CoCl_2 \cdot 6H_2O$ (0.180 g, 0.756 mmol) and Me_3tpa (0.251 g, 0.758 mmol) to give a dark green solid (0.546 g, 84%) which was recrystallized by slowly cooling a hot ethanolic solution to obtain **4a** as a dark green microcrystalline solid that analyzed as hygroscopic (**4a**·H_2O). Single crystals suitable for X-ray diffraction were also obtained by cooling an ethanolic solution, *pp*-[{Co(Me_3tpa)}$_2$(Br_4spiro)]$(PF_6)_2 \cdot x$EtOH (**4a**·*x*EtOH, x = 2–3). Anal. Calcd for $C_{63}H_{66}N_8O_5Co_2Br_4P_2F_{12}$: C, 43.42; H, 3.82; N, 6.43. Found: C, 43.94; H, 3.28; N, 5.91. TGA data is consistent with the presence of solvent. HRMS (ESI-QTOF) *m/z*: M^{2+} calcd for $C_{63}H_{64}N_8O_4Br_4Co_2$, 717.0209; found, 717.0176. IR (KBr) $\bar{\nu}_{max}$: 1607 (m), 1578 (w), 1496 (s), 1454 (s), 843 (vs), 557 (s) cm^{-1}. UV/vis (acetonitrile) λ_{max} (ε): 420 (5370), 538 (1990sh), 614 (2910), 695 (2020sh), 844 (1130sh), 972 nm (674sh mol L^{-1} cm^{-1}).

[{Zn(Me$_3$tpa)}$_2$(Br$_4$spiro)](PF$_6$) (**5a**). A methanolic (20 mL) solution of $Br_4spiroH_4$ (65.6 mg, 0.100 mmol) was deprotonated with triethylamine (61.6 µL, 0.442 mmol) and added to a methanolic (90 mL) solution of $Zn(OAc)_2 \cdot 2H_2O$ (43.4 mg, 0.198 mmol) and Me_3tpa (66.4 mg, 0.200 mmol). The yellow suspension was bubbled with a stream of compressed air for 1 h until it became bright green. The suspension was gravity filtered and the crude product was precipitated from the green filtrate by dropwise addition of a saturated aqueous potassium hexafluorophosphate solution. The crude solid was collected by vacuum filtration, washed with diethyl ether (3 × 5 mL) and allowed to air dry to give a bright green solid (0.117 g, 74%) which was recrystallized twice

by layering of an acetone solution with diethyl ether to give **5a**·4.4H_2O as a bright green microcrystalline solid. Single crystals suitable for X-ray diffraction were obtained from slow evaporation of an acetone/toluene solution, *pp*-[{Zn(Me_3tpa)}$_2$(Br_4spiro)](PF_6)·2tol (**5a**·2tol). Anal. Calcd for $C_{63}H_{72.8}N_8O_{8.4}Zn_2Br_4PF_6$: C, 45.26; H, 4.39; N, 6.70. Found: C, 45.74; H, 4.12; N, 6.19. TGA data show the onset of desolvation at 25 °C and are consistent with 4.4 H_2O solvate per molecule, lost over one step centered at 41 °C. IR (KBr) $\bar{\nu}_{max}$: 1606 (m), 1579 (w), 1519 (s), 1455 (s), 1327 (w), 1248 (m), 1225 (sh), 845 (s), 557 (m) cm^{-1}. UV/vis/NIR (acetonitrile) λ_{max} (ε): 416 (1770sh), 433 (3480), 702 (309sh), 803 (414sh), 872 (456sh), 974 (360sh), 1494 nm (136 mol L^{-1} cm^{-1}).

[{Zn(Me$_3$tpa)}$_2$(Br$_4$spiro)](PF$_6$)$_2$ (**6a**). Crude **5a** (0.295 g, 0.185 mmol) and recrystallized ferrocenium hexafluorophosphate (61.2 mg, 0.185 mmol) were suspended in toluene (100 mL) under a nitrogen atmosphere and sonicated for 2 hours and then stirred overnight. The dark green solid was collected by vacuum filtration and washed with toluene (4 × 2 mL) and diethyl ether (3 × 2 mL) and then air dried to afford crude **6a** (0.314 g, 98%). The product was recrystallized from acetone/toluene layering to give **6a**·0.5tol as a brownish green solid. The solid sample of **6a**·0.5tol appeared unstable over several weeks and precluded the collection of reliable magnetic susceptibility data. Single crystals suitable for X-ray diffraction were obtained by layering a dichloromethane solution with toluene to give *pd*-[{Zn(Me_3tpa)}$_2$(Br_4spiro)](PF_6)$_2$·tol (**6a**·tol). Anal. Calcd for $C_{66.5}H_{68}N_8O_4Zn_2Br_4P_2F_{12}$: C, 44.78; H, 3.84; N, 6.28. Found: C, 44.26; H, 4.50; N, 6.27. TGA data are consistent 0.5 toluene molecules per complex, and pyrolysis-GCMS confirms toluene (m/z 91) is lost at 130 °C. IR (KBr) $\bar{\nu}_{max}$: 1607 (s), 1580 (m), 1523 (vs), 1455 (s), 844 (vs), 558 (s) cm^{-1}. UV/vis (acetonitrile) λ_{max} (ε): 405 (3380sh), 423 (5290), 716 (525sh), 800 (718sh), 870 (777), 978 nm (539sh mol L^{-1} cm^{-1}).

X-ray Data Collection and Structure Solution. Data for $Br_4spiroH_4 \cdot 2Et_2O$ and **2b**$_{pd}$·3.9acetone were collected at 130 K using a Rigaku Oxford Diffraction SuperNova Dual Wavelength diffractometer with mirror monochromated Cu-Kα radiation (λ = 1.5418 Å). Data for **4a**·*x*EtOH were collected on a Rigaku XtaLAB Synergy-S Dual Microfocus X-ray diffractometer using Cu-Kα radiation at 100–300 K in 50 K increments. Data for **2a**·2.5MeOH, **2b**$_{pp}$·7acetone and **3a**·4.5dioxane were collected at the MX1 beamline[6] and **5a**·2tol and **6a**·tol were collected at the MX2 beamline[7] at the Australian Synchrotron, fitted with a silicon double crystal monochromator and Oxford Instruments CryoJet 5 cryostat. Data were collected at 100 K using radiation tuned to approximately Mo-Kα radiation (λ = 0.7108 Å). Crystallographic data is tabulated for $Br_4spiroH_4 \cdot 2Et_2O$ (Table S1), **2a**·2.5MeOH, **2b**$_{pp}$·7acetone, **3a**·4.5dioxane, **5a**·2tol and **6a**·tol (Table S2), and **4a**·*x*EtOH (Table S3).

Table S1. Crystallographic data for $Br_4spiroH_4 \cdot 2Et_2O$

$Br_4spiroH_4 \cdot 2Et_2O$			
T/K	130.0(1)	ρ_{calcd}/g cm^{-3}	1.681
formula	$C_{29}H_{40}O_6Br_4$	μ/mm^{-1}	6.501
fw/g mol^{-1}	804.25	reflns measd	31230
cryst syst	orthorhombic	unique reflns	3358
space group	*Pbcn*	data/restraints/param	3358/0/184
a/Å	18.3615(2)	R_{int}	0.0412
b/Å	7.57018(7)	R_1 [$I > 2\sigma(I)$]	0.0227
c/Å	22.8673(2)	wR_2 (all data)	0.0600
V/Å^3	3178.56(5)	GOF on F^2	1.107
Z	4	$\Delta\rho_{max/min}$/e Å^{-3}	0.43/–0.35
Z'	0.5		

Table S2. Crystallographic data for compounds **2a**·2.5MeOH, **2b$_{pp}$**·7acetone, **2b$_{pd}$**·3.9acetone, **3a**·4.5dioxane, **5a**·2tol and **6a**·tol

	2a·2.5MeOH	**2b$_{pp}$**·7acetone	**2b$_{pd}$**·3.9acetone	**3a**·4.5dioxane	**5a**·2tol	**6a**·tol
T/K	100(2)	100(2)	130.0(1)	100(2)	100(2)	100(2)
formula	$C_{59.5}H_{62}N_8O_{6.5}F_{12}P_2Co_2Br_4$	$C_{78}H_{94}N_8O_{19}Co_2Cl_2Br_4$	$C_{68.58}H_{75.16}N_8O_{15.86}Co_2Cl_2Br_4$	$C_{79}H_{96}N_8O_{13}F_{12}P_2Co_2Br_4$	$C_{77}H_{80}N_8O_4F_6PZn_2Br_4$	$C_{70}H_{72}N_8O_4F_{12}P_2Zn_2Br_4$
fw/g mol^{-1}	1720.61	1956.01	1773.64	2093.07	1776.84	1829.67
cryst syst	orthorhombic	triclinic	triclinic	orthorhombic	monoclinic	triclinic
space group	*Pbcn*	$P\bar{1}$	*P*1	*Iba*2	$P2_1/c$	$P\bar{1}$
a/Å	21.600(4)	17.127(3)	13.4672(4)	17.948(4)	20.821(4)	9.474(2)
b/Å	15.000(3)	19.360(4)	15.7188(4)	20.058(4)	23.729(5)	16.711(3)
c/Å	20.220(4)	25.008(5)	20.5224(5)	22.915(5)	15.968(3)	24.172(5)
α/deg	90	84.20(3)	111.532(2)	90	90	84.25(3)
β/deg	90	81.18(3)	90.341(2)	90	106.12(3)	87.61(3)
γ/deg	90	89.83(3)	109.649(3)	90	90	79.98(3)
V/Å^3	6551(2)	8151(3)	3764.1(2)	8249(3)	7579(3)	3749(1)
Z	4	4	2	4	4	2
Z′	0.5	2	2	0.5	1	1
ρ_{calcd}/g cm^{-3}	1.744	1.594	1.565	1.685	1.557	1.621
μ/mm^{-1}	3.086	2.508	7.168	2.473	2.832	2.897
reflns measd	152165	121942	29829	48401	87262	68941
unique reflns	6225	30741	18197	7484	13624	19220
data/restraints/ param	6225/54/427	30741/58/ 1587	18197/156/ 1894	7484/107/ 482	13624/108/ 826	19220/73/ 927
R_{int}	0.0985	0.0716	0.0220	0.1375	0.1060	0.0569
R_1 [$I > 2\sigma(I)$]	0.0681	0.0645	0.0371	0.0669	0.0725	0.0585
wR_2 (all data)	0.1996	0.2212	0.0980	0.1794	0.2281	0.1763
GOF on F^2	1.019	1.079	1.046	1.053	0.927	1.085
$\Delta\rho_{max/min}$/e Å^{-3}	1.57/–0.75	1.19/–0.54	0.89/–0.55	1.03/–1.27	0.97/–0.82	1.19/–1.56
Flack	n/a	n/a	0.482(4)	0.10(2)	n/a	n/a

Table S3. Variable-temperature crystallographic data for **4a**·*x*EtOH

	100 K	**150 K**	**200 K**	**250 K**	**300 K**
*x*EtOH	2	3	2.5	3	2
formula	$C_{67}H_{76}N_8O_6F_{12}P_2Co_2Br_4$	$C_{69}H_{82}N_8O_7F_{12}P_2Co_2Br_4$	$C_{68}H_{79}N_8O_{6.5}F_{12}P_2Co_2Br_4$	$C_{69}H_{82}N_8O_7F_{12}P_2Co_2Br_4$	$C_{67}H_{76}N_8O_6F_{12}P_2Co_2Br_4$
fw/g mol^{-1}	1816.79	1862.86	1839.83	1862.86	1816.79
cryst syst	orthorhombic	orthorhombic	orthorhombic	orthorhombic	orthorhombic
space group	*Pnna*	*Pnna*	*Pnna*	*Pnna*	*Pnna*
a/Å	26.0119(3)	26.0240(3)	26.0671(3)	26.1933(4)	26.2505(5)
b/Å	14.2861(2)	14.4389(1)	14.5259(2)	14.6636(2)	14.6662(4)
c/Å	20.1208(2)	20.3551(2)	20.4819(3)	20.6104(3)	20.6389(5)
V/Å^3	7477.1(2)	7648.6(1)	7755.4(2)	7916.2(2)	7945.9(3)
Z	4	4	4	4	4
Z′	0.5	0.5	0.5	0.5	0.5
T/K	100.0(1)	150.0(1)	200.0(1)	250.0(1)	300.0(1)
ρ_{calc}/g cm^{-3}	1.614	1.618	1.576	1.563	1.519
μ/mm^{-1}	7.116	6.982	6.873	6.746	6.696
reflns measd	57008	46089	64622	48187	48698
unique reflns	7939	8071	8248	8369	8401
data/restraints /param	7939/0/434	8071/121/480	8248/67/480	8369/55/480	8401/55/480
R_{int}	0.0538	0.0358	0.0574	0.0446	0.0493
R_1 [$I > 2\sigma(I)$]	0.0711	0.1097	0.0869	0.0574	0.0621
wR_2 (all data)	0.2029	0.3139	0.2926	0.1926	0.203
GOF on F^2	1.033	1.124	1.116	1.119	1.056
$\Delta\rho_{max/min}$/e Å^{-3}	1.08/–0.95	2.71/–2.84	1.25/–1.28	1.02/–0.79	0.91/–0.47

Crystals were transferred directly from the mother liquor into a cryoprotective oil and then immediately mounted on the diffractometer at the data collection temperature to prevent solvent loss. Individual crystals of **4a**·*x*EtOH were used for each variable temperature collection with the exception of 150 K and 200 K, as crystals suffered radiation damage if used for multiple

collections. The data for **2b$_{pd}$**·3.9acetone, **4a**·*x*EtOH and Br$_4$spiroH$_4$·2Et$_2$O were processed using CrysAlisPro,[8] while data reduction for **2b$_{pp}$**·7acetone, **3a**·4.5dioxane, **5a**·2tol and **6a**·tol were performed with XDS,[9] using moderate multi-scan absorption correction in SADABS.[10] Data reduction for **2a**·2.5MeOH was performed in XDS with multiple scans merged in XSCALE.[10] All structures were solved using the intrinsic phasing routine in SHELXT and refined using a full-matrix least square procedure based upon F^2 using SHELXL within OLEX2.[11-13] For all structures, the positions of all non-hydrogen atoms were refined using anisotropic displacement parameters. Hydrogen atoms were placed geometrically, and their positions were constrained to geometrical estimates using the riding model.

In view of a space group ambiguity, specific details on the solution of the structure of **2b$_{pp}$**·7acetone are discussed. *E*-statistics suggested the compound **2b$_{pp}$**·7acetone crystallized in the non-centrosymmetric space group *P*1. Attempts to solve the structure in a centrosymmetric space group, using several structure solution packages (SHELXS, SHELXT, OLEX and Superflip), were not successful.[12-15] However, a solution in the non-centrosymmetric space group *P*1 occurred readily, with two dinuclear molecules comprising the asymmetric unit, which, for *P*1, is the entire unit cell. Attempts to find a center of symmetry within the molecule were unsuccessful. Neither CIFCheck nor the ADDSYMM function in Platon were able to detect any center of symmetry.[16-18] Attempts to refine the structure as a disordered centrosymmetric structure were also not successful. Accordingly, the refinement was continued in the space group *P*1 with a satisfactory convergence. The value of the Flack parameter indicates that the selected crystal was a racemic twin, with individual components of 0.518(4) and 0.482(4).

Two molecules of acetone in **2b$_{pd}$**·3.9acetone and a molecule of dioxane in **3a**·4.5dioxane were able to be located. Refinement was carried out with the solvent molecules being restrained

to ideal geometry, with the displacement parameters of some of the atoms being restrained to near isotropic values. Crystals of **3a**·4.5dioxane, **4a**·*x*EtOH, **5a**·2tol and **6a**·tol displayed highly disordered solvent which could not be readily modeled. Accordingly, refinement of these structures was carried out with the OLEX2 solvent mask routine,[13] which determined the volume of the solvent void and the electron density within the void.

Disorder of the perchlorate anions was observed in $\mathbf{2b_{pp}}$·7acetone and $\mathbf{2b_{pd}}$·3.9acetone. Four anions in $\mathbf{2b_{pd}}$·3.9acetone and one anion in $\mathbf{2b_{pp}}$·7acetone were restrained to have ideal geometry and were modelled over two orientations with the anisotropic displacement parameters of the atoms being restrained to have similar and near-isotropic values.

Disorder of the hexafluorophosphate anions was observed in **2a**·2.5MeOH, **4a**·*x*EtOH (*T* = 150–300 K), **5a**·2tol and **6a**·tol. In the structures of **3a**·4.5dioxane and **4a**·*x*EtOH (*T* = 150–300 K), PF_6^- anions were modelled over three orientations with each component restrained to ideal geometry and with the anisotropic displacement parameters of equivalent atoms being constrained to be equal. The PF_6^- anion in **2a**·2.5MeOH was similarly modelled over two orientations. The PF_6^- anion in **5a**·2tol was disordered over two orientations with both components restrained to ideal geometry and with the fluorine atoms being restrained to have similar anisotropic displacement parameters. One of the PF_6^- anions in **6a**·tol was disordered over a center of symmetry; the anion was modelled using three components, with the central phosphorus atoms constrained to the same position and the anisotropic displacement parameters of the fluorine atoms restrained to have similar, near-isotropic values. In structures of **2a**·2.5MeOH, **3a**·4.5dioxane, **4a**·*x*EtOH (*T* = 150, 200 K) and **5a**·2tol some of the carbon atoms belonging to Me_ntpa and Br_4spiro appeared significantly disordered and so the anisotropic displacement parameters were constrained to have similar or near-isotropic values.

X-ray powder diffraction data were measured on the Rigaku XtaLAB Synergy-S Dual Microfocus X-ray diffractometer using Cu-Kα radiation. Measurements were performed at 100 K, with exception of **4a**·H_2O, for which measurements were taken at 50 K intervals between 100 and 300 K. Powder samples were prepared by crushing the samples and loading into a 0.3 mm borosilicate glass capillary. Data were collected to $2\theta = 80°$ with an exposure time of 60 s per frame and processed using CrysAlisPro software.[19-20]

Electronic Absorption Spectroscopy. Ultraviolet-visible (UV-vis) absorption spectra were recorded on an Agilent Cary 60 UV-Vis spectrophotometer in the range 350–1000 nm. Near infra-red (NIR) absorption spectra were performed on a Perkin-Elmer Lambda 1050 UV/Vis/NIR spectrophotometer in the range 800–2200 nm. UV-vis-NIR measurements were recorded for acetonitrile (MeCN) solutions of **1a**–**6a**, a 1,2-dichloroethane solution of **5a** and a chlorobenzene solution of **5a**. UV-vis measurements were also recorded for tetrahydrofuran (THF) solutions of **1a**, **2a** and **4a**. Near infra-red spectra in MeCN were corrected for spurious bands at 1408 nm and 1908 nm which also appeared in in the blank MeCN spectrum. The NIR spectra of **5a** was corrected at low energy (1800–2200 nm) for a discontinuity in absorbance at 1800 nm corresponding to a change in detector.

Electrochemistry. Prior to electrochemical measurements, the stability of all compounds in MeCN over 4–5 h was confirmed: **1a** is stable under a nitrogen atmosphere only (Figure S17 and Figure S18) and **2a**–**6a** are air-stable (Figure S17). Electrochemical measurements were performed in MeCN (**1a**–**6a**) and THF (**1a**, **2a** and **4a**) at room temperature using a standard three-electrode configuration connected to an eDAQ computer-controlled potentiostat. Measurements were performed under a continuous nitrogen flow. For cyclic voltammetry measurements the three-electrode system consisted of a 1.0 mm diameter glassy carbon electrode (Cypress Systems),

a platinum wire auxiliary electrode and a commercially available Ag/AgCl reference electrode (eDAQ). For steady state voltammetry measurements, the working electrode was replaced with a 3.0 mm diameter glassy carbon rotating disk electrode with external controller (Metrohm). Analyte solutions of 1.0 mM were prepared in solvent containing 0.25 M Bu_4NPF_6 as the supporting electrolyte.

All potentials have been referenced *versus* the ferrocene/ferrocenium redox couple, measured immediately afterwards. The cyclic voltammetry (CV) midpoint potentials (E_m) are calculated by taking the average of the anodic and cathodic peak potentials (E_p). The half-wave potentials ($E_{1/2}$) are calculated as the potential at half the limiting current (i_L). Reversible processes are identified by peak-to-peak separations (ΔE_p) close to the value measured under the same conditions for ferrocene at a scan rate of 100 mV s^{-1} (68–81 mV in MeCN, 80–98 mV in THF).

Solid-State Magnetic Measurements. Magnetic measurements were performed on a Quantum Design MPMS-XL SQUID magnetometer. Microcrystalline samples of **1a**·CH_2Cl_2, **2a**·$4H_2O$, **3a** and **4a**·H_2O were loaded into polypropylene bags and the bags were heat sealed inside a glove box. The samples were finely crushed inside the bag, rolled up tightly and packed into a drinking straw. Ferromagnetic impurity checks were performed for each sample at 100 K by sweeping the field (0–10 kOe): linearity in plots indicates the lack of significant magnetic impurities (Figure S15). Magnetic susceptibility data were acquired under the application of a 1 kOe field for paramagnetic samples (**1a**·CH_2Cl_2 and **4a**·H_2O), a 1.5 kOe field for **2a**·$4H_2O$ and a 10 kOe field for **3a** in the temperature range 2–360 K. Magnetic susceptibility measurements were corrected for the diamagnetic contribution of the polypropylene bag and diamagnetic contribution of the samples using Pascal's constants.[21]

Other Measurements. Elemental analyses were performed by the Campbell Microanalytical Laboratory, Chemistry Department, University of Otago, New Zealand. High resolution mass spectra (HRMS) were performed on an Agilent 6520 Accurate-Mass Q-TOF spectrometer. Thermogravimetric analyses were performed on a Mettler Toledo thermal analyzer using a ramp rate of 5 °C min^{-1} up to a maximum temperature of 400 °C. Pyrolysis-gas chromatography mass spectrometry (GCMS) was performed by TRACEES at the University of Melbourne. Infrared spectra (KBr disk) were recorded on a Bruker Tensor 27 FTIR spectrometer. All ^{1}H NMR spectra were acquired on a Varian MR400 400 MHz spectrometer and referenced to residual protic solvent.

Density Functional Theory (DFT) Calculations. The DFT calculations were performed using the Gaussian 16 program package[22] with the UTPSSh functional[23-24] and the 6-311++G(d,p) basis set. This methodology provides a good reproduction of the energies and magnetic properties of magnetically-bistable transition metal compounds.[25-32] The stationary points on the potential energy surfaces were located by full geometry optimization with calculation of force constants and were checked for the stabilities of the DFT wavefunction. The estimation of exchange coupling parameters J (in cm^{-1}; $\hat{H} = -2JS_1 \cdot S_2$) was carried out by calculation of all possible charge distributions using the "broken symmetry" (BS) formalism[33] with the generalized spin-projection method developed by Yamaguchi.[34] Structural visualizations were prepared using the ChemCraft[35] software with the calculated atomic coordinates as input parameters. Calculations on cationic complexes $\mathbf{2_{pp}}^{2+}$, $\mathbf{3}^{2+}$ and $\mathbf{4}^{2+}$ incorrectly reproduce the relative energies of the different charge distributions by underestimating the stabilization energy of the {Co^{III}-cat-cat-Co^{III}} state, as it was shown previously.[26,29] For this reason, magnetic properties were studied for the systems including counter-ions.

For compound **3a**, the methyl groups of Me_2tpa are approximately equally disordered over three sites. We performed calculations on $\mathbf{3}^{2+}$ with various methyl group positions and with the {Co^{III}-cat-cat-Co^{III}} charge distribution. The energy difference of the isomers did not exceed 1.5 kcal mol^{-1} and so further calculations were performed on **3a** with the methyl groups in the exterior and interior positions (Figure S12).

Literature Ligands

Chart S1. Bis(dioxolene) ligands used as linkers in dinuclear cobalt complexes that display VT in the literature.[36-39]

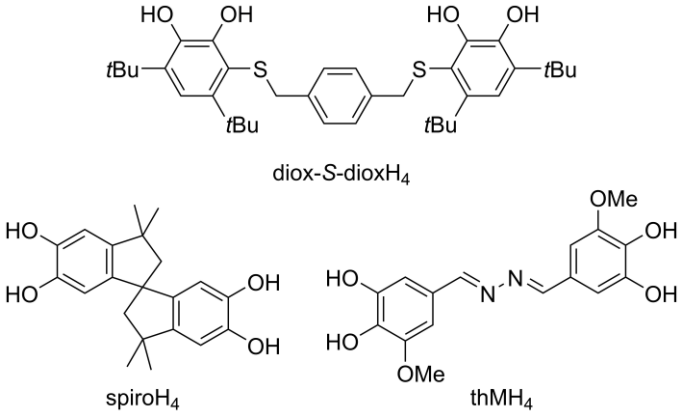

Powder X-ray Diffraction

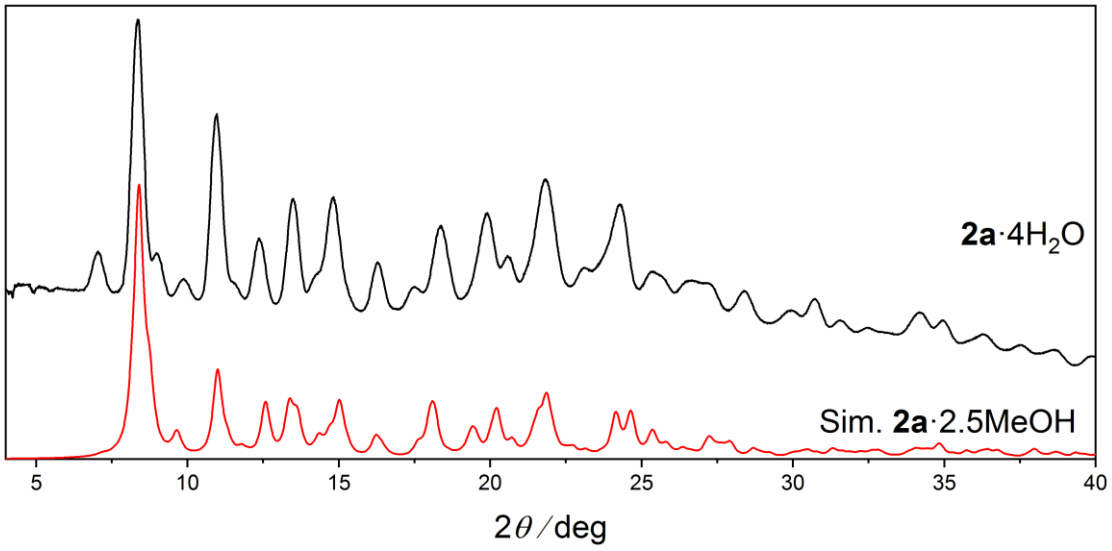

Figure S1. Experimental PXRD pattern of **2a**·4H_2O at 100 K (black) and simulated PXRD pattern from crystal structure of **2a**·2.5MeOH at 100 K (red).

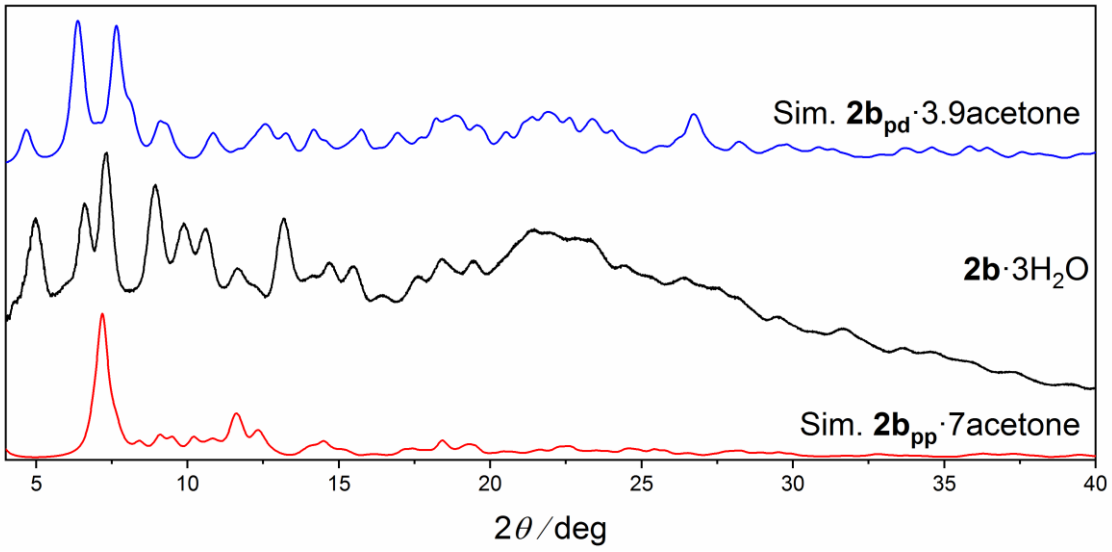

Figure S2. Experimental PXRD pattern of **2b**·3H_2O at 100 K (black) and simulated PXRD patterns from crystal structures of $\mathbf{2b_{pp}}$·7acetone at 100 K (red) and $\mathbf{2b_{pd}}$·3.9acetone at 130 K (blue).

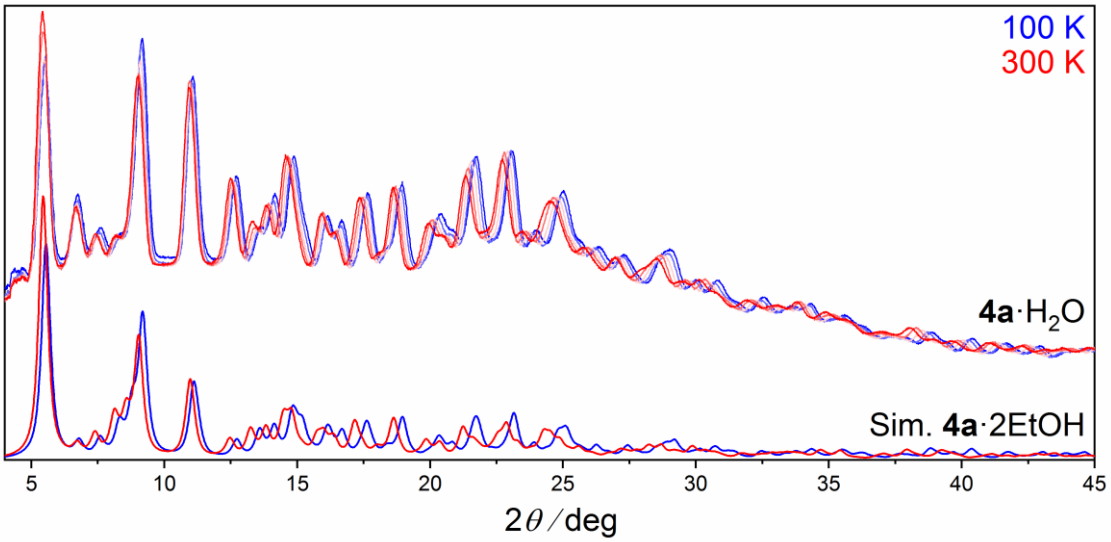

Figure S3. (Top) Experimental PXRD patterns at 50 K intervals between 100 K (blue) and 300 K (red) for **4a**·H_2O. (Bottom) Simulated PXRD patterns from crystal structures of **4a**·2EtOH at 100 K (blue) and 300 K (red).

Thermogravimetric Analysis

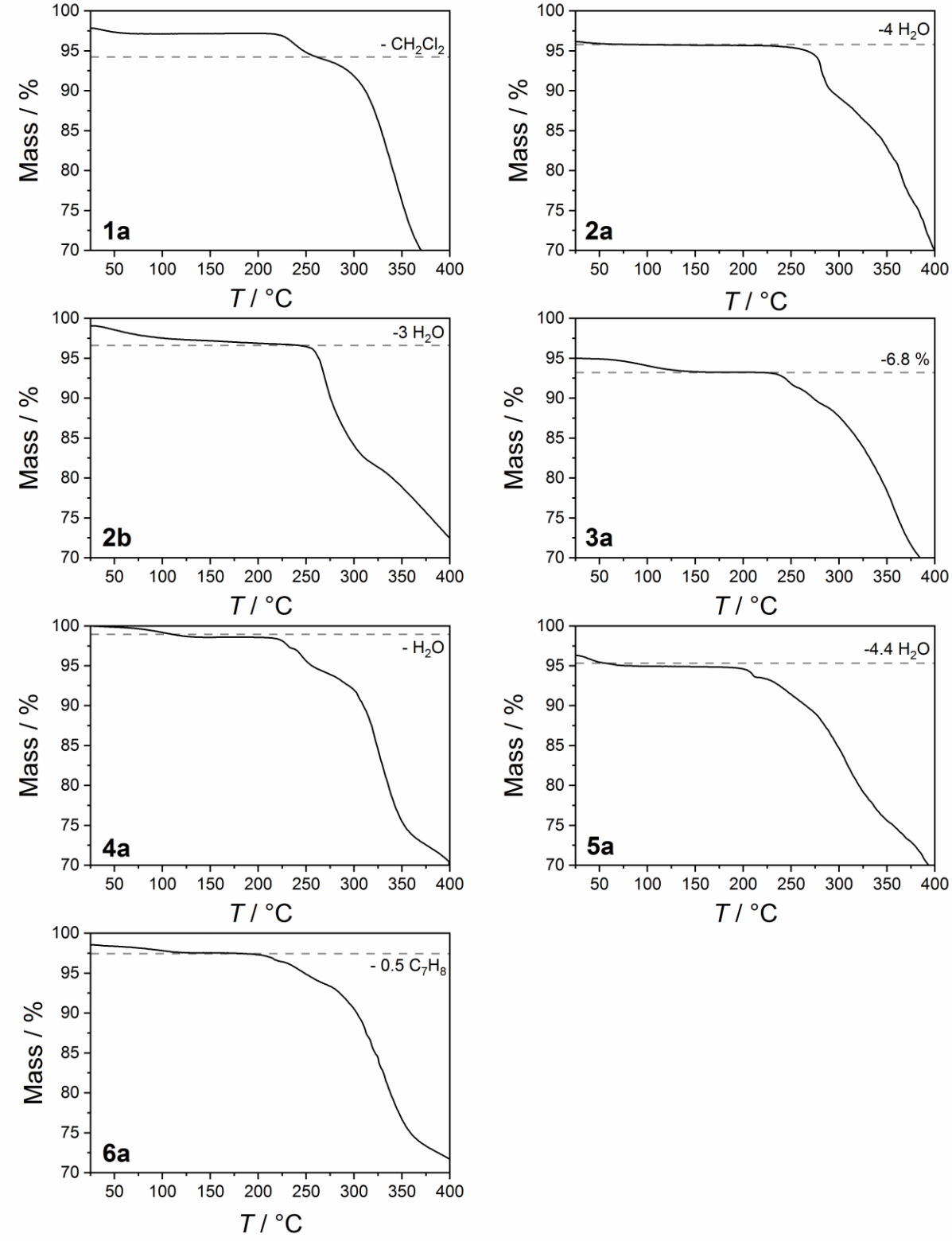

Figure S4. TGA data for **1a**–**6a** and **2b**.

Infrared Spectroscopy

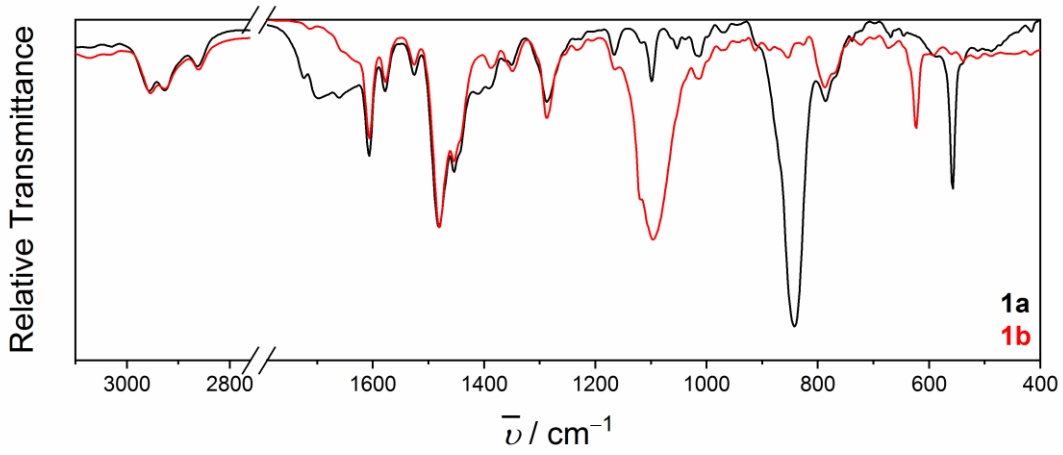

Figure S5. IR spectra (KBr disk) of **1a** (black) and **1b** (red).[38]

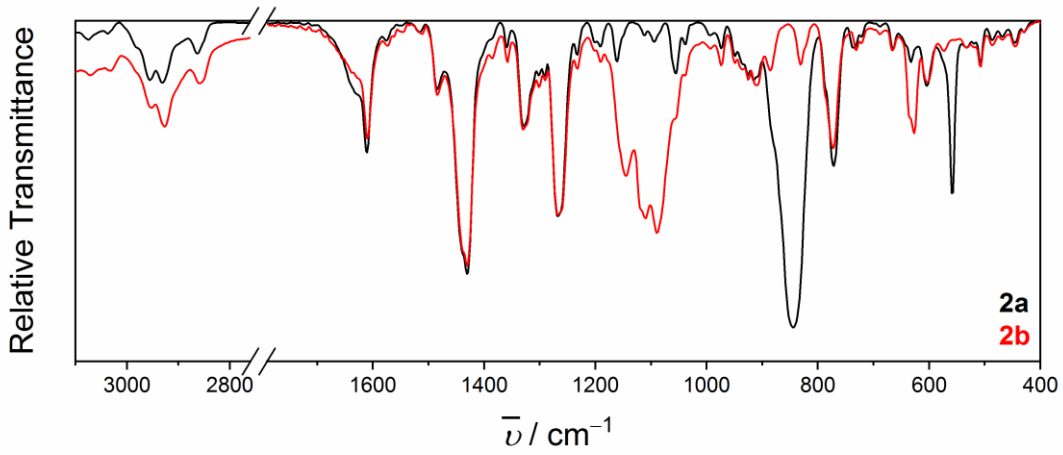

Figure S6. IR spectra (KBr disk) of **2a** (black) and **2b** (red).

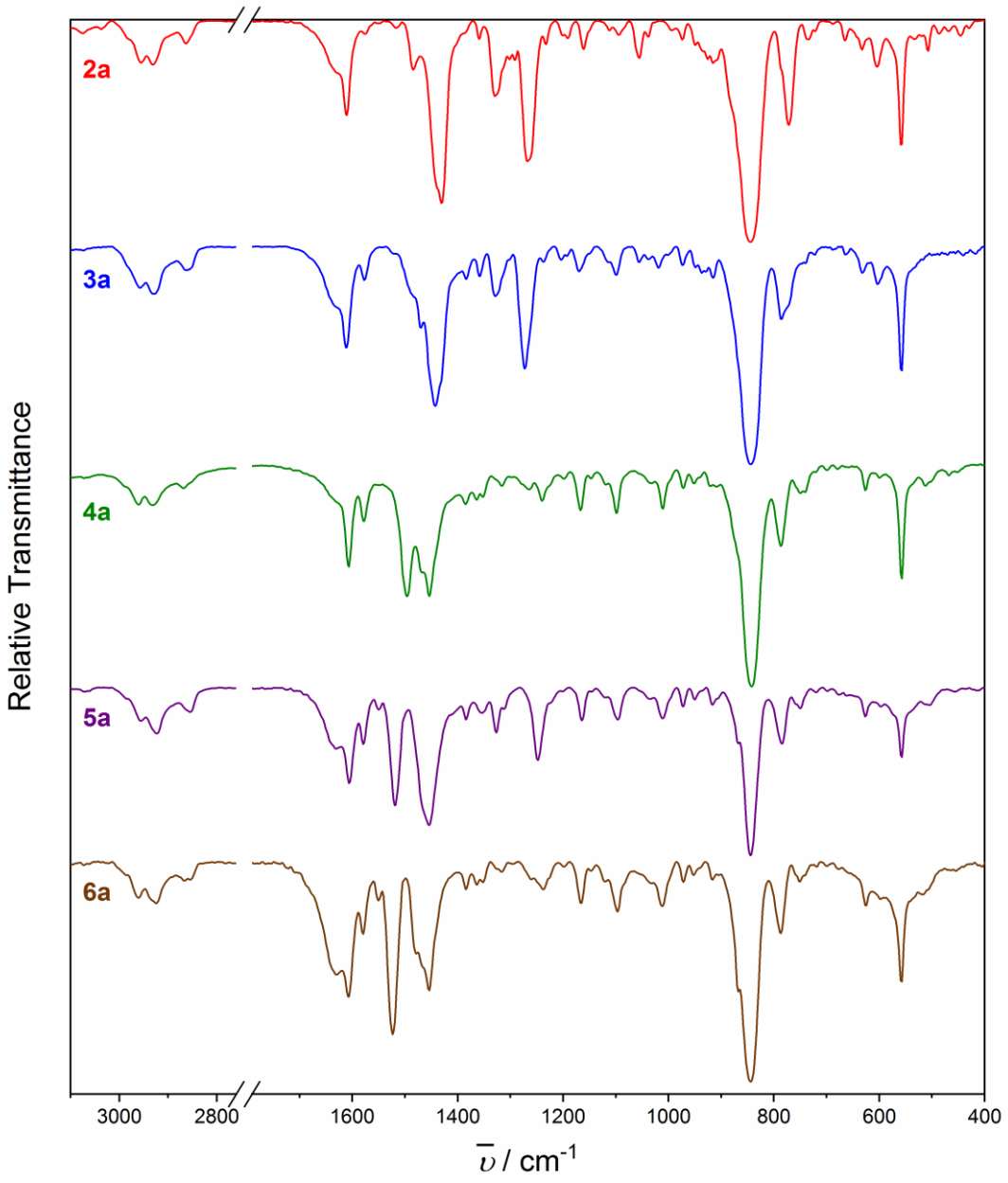

Figure S7. IR spectra (KBr disk) of **2a** (red), **3a** (blue), **4a** (green), **5a** (purple) and **6a** (brown).

Table S4. Selected IR (cm^{-1}) assignments of compounds **1a-6a**.

Moiety and Assignment		1a	2a	3a	4a	5a	6a	Ref [a]
tpa	ν(C=C)	1610 (m)	1611 (m)	1612 (m)	1607 (m)	1606 (m)	1607 (s)	40
tpa	ν(C=N)	1578 (w)	1576 (w)	1577 (w)	1578 (w)	1579 (w)	1580 (m)	40
SQ	ν(C-C)	1480 (s)	-	-	1496 (s)	1519 (s)	1523 (vs)	41*b*
SQ	ν(C=O) + ν(C=C) + δ(C-H) [c]	1454 (m)	-	-	1454 (s)	1455 (s)	1455 (s)	38,40
cat	ν(C-O) + δ(C-H) [c]	1445 (sh)	1430 (vs)	1443 (s)	-	-	-	38,40
cat	ν(C=O) + ν(C=C) + δ(C-H) [c,d]	1412 (w)	-	-	-	-	-	40
cat	ν(C-O) + ν(C=C) + ν(C-C)	-	1329 (m)	1329 (w)	-	1327 (w)	-	40,42
cat	skeletal diox	1287 (m)	1268 (s)	1273 (s)	-	1248 (m) [e]	-	38,40,42
cat	ν(C-O) + ν(C-C)	-	1233 (w)	1237 (w)	-	-	-	40,42
PF_6^-	ν(P-F)	843 (vs)	844 (vs)	845 (vs)	843 (vs)	845 (s)	844 (vs)	43
PF_6^-	δ(P-F) + ν(P-F)	557 (s)	558 (s)	557 (s)	557 (s)	557 (m)	558 (s)	43

[a] Catecholate, semiquinonate and tpa assignments are based on literature DFT,[40] unless specified otherwise. [b] Assignment is not based on DFT results. Band is shifted to lower wavenumbers in cobalt compounds **1a** and **2a** due to π-backdonation that does not occur in zinc compounds **5a** and **6a**. [c] Only compound **1a** contains aromatic protons. [d] Band only appears in the presence of aromatic protons. [e] Bands show a significant shift from expected value and assignment is tentative.

Additional Structural Data – $Br_4spiroH_4 \cdot 2Et_2O$

The crystal data and structural data for $Br_4spiroH_4 \cdot 2Et_2O$ are reported in Table S1 and Table S5; $Br_4spiroH_4 \cdot 2Et_2O$ crystallizes in the orthorhombic space group *Pbcn*, with half of the $Br_4spiroH_4$ molecule and one diethyl ether molecule present in the asymmetric unit (Figure S8). The other half of $Br_4spiroH_4$ is symmetry related by a C_2 rotation axis through the spirocyclic carbon (C11). Brown *et al.* have defined an empirical metrical oxidation state (MOS) parameter using a least squares fitting of C-C and C-O bond lengths, as suggested by Carugo, in order to assign an apparent oxidation state to dioxolene ligands (Table S5).[44-45] The expected catechol oxidation state is confirmed by a MOS value of –2.03(9). In the uncoordinated ligand, the resting dihedral angle between the two dioxolene planes is 79.03(3)°, although this may be affected by hydrogen bonding between the hydroxyl groups and diethyl ether.

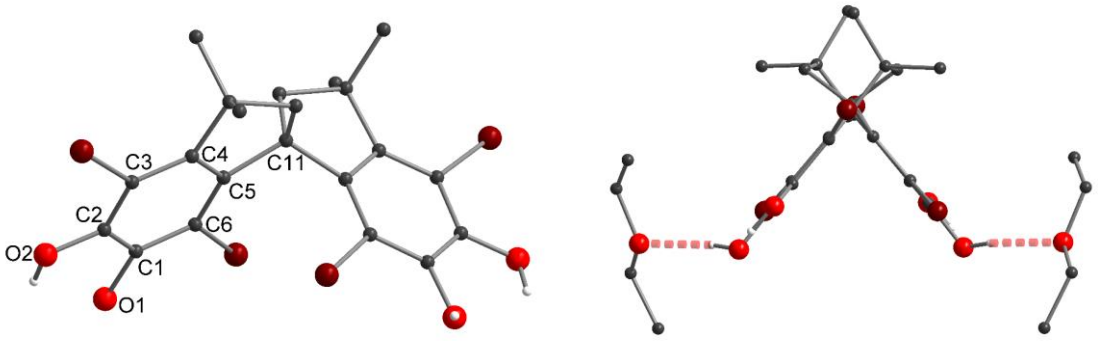

Figure S8. Structure of $Br_4spiroH_4 \cdot 2Et_2O$ showing proligand only (*left*) and hydrogen-bonding with diethyl ether solvate (*right*). Color code: carbon, black; oxygen, red; bromine, brown; hydroxyl hydrogen, white.

Table S5. Structural data for $Br_4spiroH_4 \cdot 2Et_2O$

$Br_4spiroH_4 \cdot 2Et_2O$	
O1-C1/Å	1.366(2)
O2-C2/Å	1.361(2)
C1-C2/Å	1.398(3)
C2-C3/Å	1.391(3)
C3-C4/Å	1.390(2)
C4-C5/Å	1.396(2)
C5-C6/Å	1.394(2)
C6-C1/Å	1.389(3)
Diox MOS [a]	–2.03(9)
Dihedral Angle/° [b]	79.03(3)

[a] Dioxolene Metrical Oxidation State as defined by Brown *et al.* ref.[44] [b] Angle between planes defined by (O1, O2, C1, C2, C3, C4, C5, C6) and intramolecular symmetry equivalent atoms.

Additional Structural Data – Dinuclear Complexes

Compounds **2a**·2.5MeOH, **3a**·4.5dioxane and **4a**·*x*EtOH crystallize in orthorhombic space groups *Pbcn*, *Iba*2 and *Pnna*, respectively. These three compounds contain only half of the dicationic cobalt complex in the asymmetric unit, with the other half being generated by rotation around the C_2 axis that passes through the spirocyclic carbon (C11; Figure 2 and Figures S9–S10). The asymmetric unit of **2a**·2.5MeOH also contains one PF_6^- anion and an average of 2.5 methanol molecules per solvent void (10 molecules per unit cell). In addition to one half of the dicationic cobalt complex, the asymmetric unit of **3a**·4.5dioxane contains an ordered 1,4-dioxane molecule and a channel along the *c*-axis containing disordered PF_6^- anion and solvent, with an average of one anion and 1.25 molecules of 1,4-dioxane per asymmetric unit (half-complex). The asymmetric unit of **4a**·*x*EtOH contains half the cationic complex, one disordered PF_6^- anion and disordered ethanol solvate (x = 2–3 depending on the individual crystal measured).

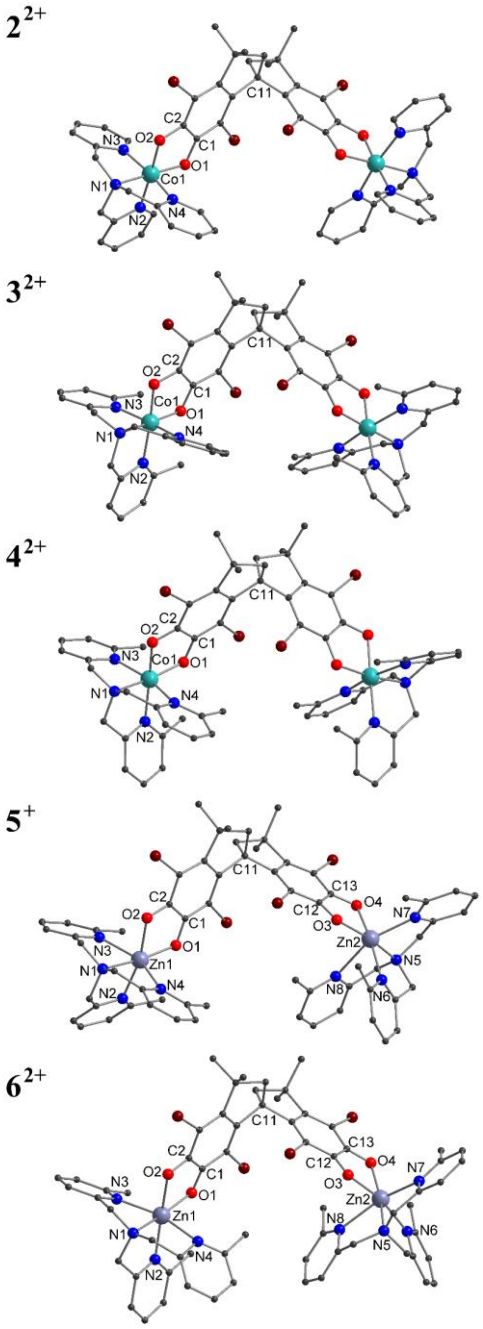

Figure S9. Complex cations in **2a**·2.5MeOH, **3a**·4.5dioxane, **4a**·2EtOH, **5a**·2tol and **6a**·tol at 100 K. Color code: carbon, black; oxygen, red; nitrogen, blue; cobalt, aqua green; bromine, brown; zinc, gray. Hydrogen atoms have been omitted for clarity.

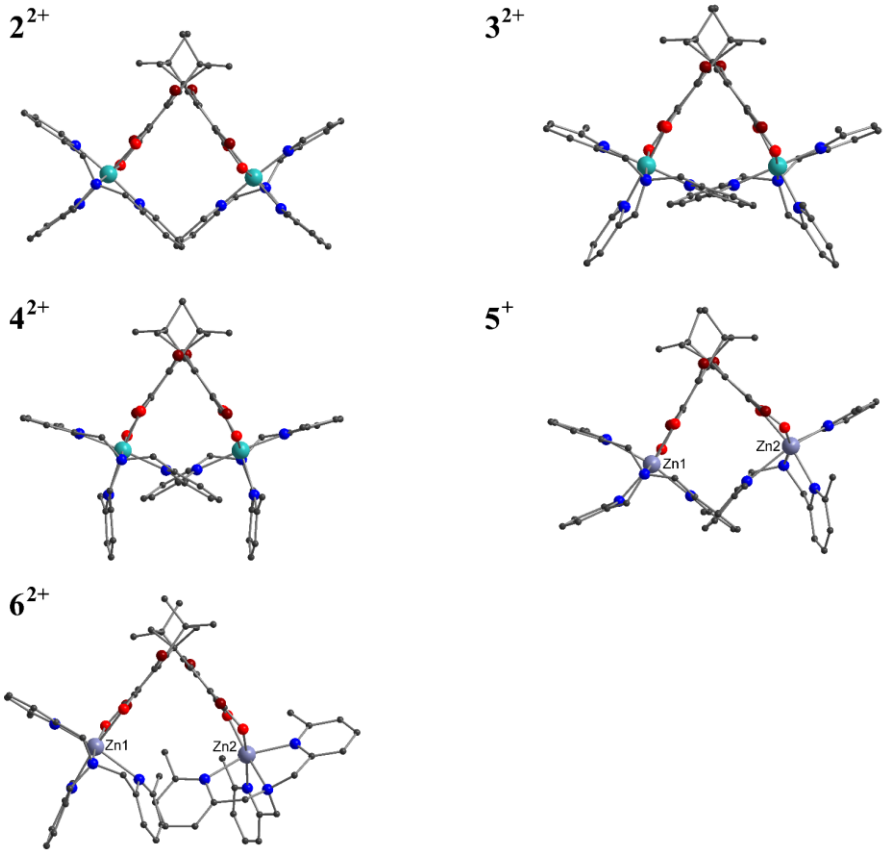

Figure S10. Complex cations in crystal structures of **2a**·2.5MeOH, **3a**·4.5dioxane, **4a**·*x*EtOH, **5a**·2tol and **6a**·tol (100 K) from a different viewing angle. Color code as per Figure S9. Hydrogen atoms are omitted for clarity.

Compound **2b** crystallizes in the triclinic space groups $P\bar{1}$ (**2b**$_{\mathbf{pp}}$·7acetone) and $P1$ (**2b**$_{\mathbf{pd}}$·3.9acetone) with two complete dinuclear cobalt complexes (***A*** and ***B***) in the asymmetric unit (Figure S11). The asymmetric unit of **2b**$_{\mathbf{pp}}$·7acetone also contains four perchlorate anions and an average of 14 acetone molecules per unit cell. The asymmetric unit of **2b**$_{\mathbf{pd}}$·3.9acetone also contains four perchlorate anions and 7.8 acetone molecules.

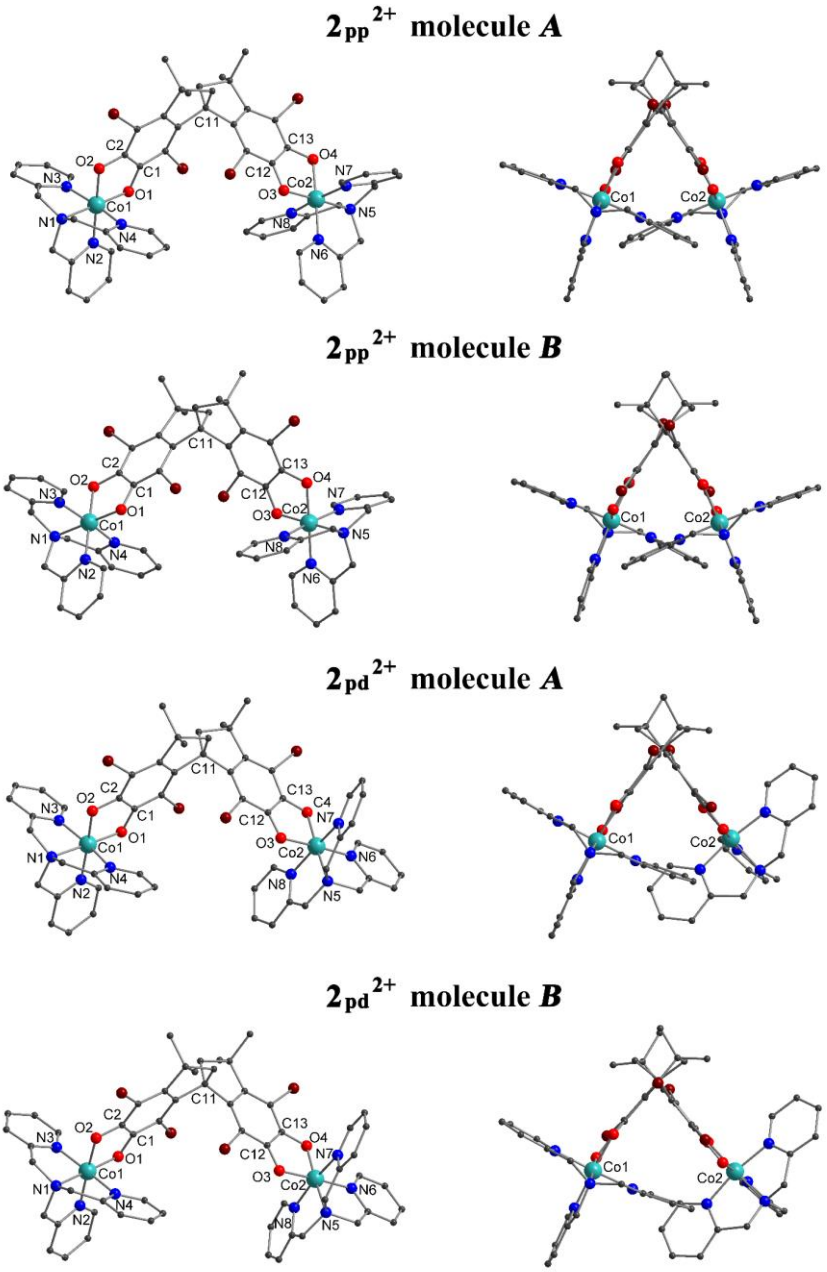

Figure S11. Complex cations in crystal structures of $\mathbf{2b_{pp}}$·7acetone (100 K) and $\mathbf{2b_{pd}}$·3.9acetone (130 K) from two viewpoints. Color code as per Figure S9: carbon, black; oxygen, red; nitrogen, blue; cobalt, aqua green; bromine, brown; zinc, gray. Hydrogen atoms are omitted for clarity.

Compounds **5a**·2tol and **6a**·tol crystallize in the monoclinic space group $P2_1/c$ and the triclinic space group $P\bar{1}$, respectively, and contain one complete dinuclear zinc complex in the asymmetric unit (Figure S10). The asymmetric unit of **5a**·2tol also contains a single PF_6^- anion (per monocationic dinuclear complex) and two disordered toluene molecules that are in a plane parallel to the *b*- and *c*-axes. The asymmetric unit of **6a**·tol contains one complete PF_6^- anion, two halves of PF_6^- anions positioned on inversion centers, and a single disordered toluene molecule in addition to the zinc complex.

In the cationic complexes $\mathbf{2}^{2+}$–$\mathbf{6}^{2+}$, the 6-coordinate metal atoms have a N_4O_2 coordination environment comprised of two *cis* O atoms from Br_4spiro, plus three pyridyl N and one tertiary amine N from Me$_n$tpa (Figure 2, Figures S9–S11). Structural isomers of the complexes are possible as the two oxygen atoms of the Br_4spiro ligand are inequivalent: O1/O3 is in close proximity to the spirocyclic carbon (*proximal*) while O2/O4 is more distant from the spirocyclic carbon (*distal*; Figure S9).[38] Complexes in **2a**·2.5MeOH, $\mathbf{2b_{pp}}$·7acetone, **3a**·4.5dioxane, **4a**·*x*EtOH and **5a**·2tol are *proximal-proximal* (*pp*) isomers as the *proximal* oxygens are *trans* to the amine nitrogen atoms of Me$_n$tpa (N1/N5). Complexes in $\mathbf{2b_{pd}}$·3.9acetone and **6a**·tol are *proximal-distal* (*pd*) isomers because at the second metal center, the *distal* oxygen (O4) is *trans* to N1 (Figures S9–S11). Thus, crystallization of **2b** from acetone/hexane or acetone/cyclohexane results in resolution of the two geometric isomers (Figure S11).

The structures of the *pp* complexes $\mathbf{2}^{2+}$–$\mathbf{5}^{+}$ are similar, with the main variation being in the orientation of the N2 pyridyl ring. For **2a**·2.5MeOH, $\mathbf{2b_{pp}}$·7acetone and **3a**·4.5dioxane, the N2 pyridyl ring is approximately co-planar with the coordinating dioxolene, with dihedral angles in the range 10–17°, but in **4a**·*x*EtOH and **5a**·2tol these pyridyl rings are significantly twisted, with the corresponding dihedral angles being in the range 37–38° and 38–44°, respectively (Figures

S9–S11). In **3a**·4.5dioxane the two methyl groups of Me_2tpa are approximately equally disordered over the interior, equatorial and exterior positions (Figure S12) with occupancies 0.724(5), 0.608(5) and 0.668(5), respectively.

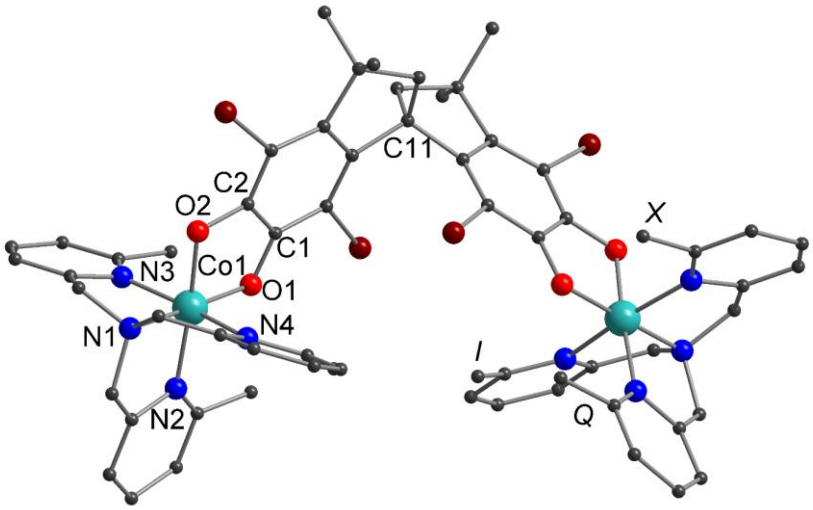

Figure S12. Complex cations in crystal structures of **3a**·4.5dioxane (100 K). Color code as per Figure S9. Labels indicate atom labels or methyl group positions: exterior, *X*; equatorial, *Q*; interior, *I*.

The intramolecular bond lengths and distortion parameters are given for **2a**·2.5MeOH, **3a**·4.5dioxane, **5a**·2tol and **6a**·tol in Table S6; $\mathbf{2b_{pp}}$·7acetone and $\mathbf{2b_{pd}}$·3.9acetone in Table S7 and **4a**·*x*EtOH in Table S8. These parameters are used to assign charge distributions as discussed in the main text.

Table S6. Selected structural data for **2a**·2.5MeOH, **3a**·4.5dioxane, **5a**·2tol and **6a**·tol at 100 K

	2a·2.5MeOH	**3a**·4.5dioxane	**5a**·2tol		**6a**·tol	
			Zn1	***Zn2***	***Zn1, p***	***Zn2, d***
M1-O1 or M2-O3/Å	1.868(4)	1.879(7)	1.981(5)	1.995(5)	1.991(3)	2.163(3)
M1-O2 or M2-O4/Å	1.896(4)	1.881(8)	2.118(4)	2.116(4)	2.211(3)	2.024(2)
M1-N1 or M2-N5/Å	1.934(6)	1.92(1)	2.099(7)	2.118(7)	2.121(3)	2.143(3)
M1-N2 or M2-N6/Å	1.913(5)	1.974(9)	2.189(5)	2.184(5)	2.139(3)	2.126(3)
M1-N3 or M2-N7/Å	1.921(6)	1.97(1)	2.331(6)	2.202(7)	2.183(3)	2.192(3)
M1-N4 or M2-N8/Å	1.907(7)	1.962(6)	2.265(5)	2.499(6)	2.418(3)	2.306(3)
O1-C1 or O3-C12/Å	1.340(7)	1.34(1)	1.302(6)	1.321(7)	1.283(4)	1.270(4)
O2-C2 or O4-C13/Å	1.348(7)	1.36(1)	1.277(8)	1.294(9)	1.276(4)	1.270(4)
C1-C2 or C12-C13/Å	1.410(9)	1.40(1)	1.450(9)	1.453(9)	1.465(5)	1.478(5)
Diox MOS [a]	–1.8(1)	–1.8(2)	–1.2(2)	–1.1(1)	–0.93(3)	–0.80(5)
SHAPE (O_h) [b]	0.163	0.275	1.901	2.076	1.577	1.513
Σ/deg [c]	34.3	40.9	105.6	103.2	97.2	104.7
Θ/deg [c]	85.2	95.0	256.9	287.6	253.6	238.8
Charge distribution [d]	{Co^{III}-cat-cat-Co^{III}}	{Co^{III}-cat-cat-Co^{III}}	{Zn^{II}-cat-SQ-Zn^{II}}		{Zn^{II}-SQ-SQ-Zn^{II}}	

[a] Dioxolene Metrical Oxidation State as defined by Brown *et al.* ref.[44] [b] SHAPE index for octahedral geometry, calculated in SHAPE 2.1 and described in text.[46-47] [c] $\Sigma = \sum_{i=1}^{12}|90 - \alpha_i|$ where α_i are the twelve cis-O/N-M-O/N angles about the cobalt atom. $\Theta = \sum_{j=1}^{24}|60 - \theta_j|$ where θ_j are the 24 unique O/N-M-O/N angles, $|\theta_j| < 120°$, measured on the projection of two triangular faces of the octahedron along their common pseudo-threefold axis.[48] Calculated using OctaDist—A program for determining the structural distortion of the octahedral complexes.[49] [d] Majority charge distribution at the indicated temperature derived from both structural and magnetic/spectroscopic studies.

Table S7. Selected structural data for $\mathbf{2b_{pp}}$·7acetone and $\mathbf{2b_{pd}}$·3.9acetone

	$\mathbf{2b_{pp}}$·7acetone *100 K*				$\mathbf{2b_{pd}}$·3.9acetone *130 K*			
Metal center	***Co1A***	***Co2A***	***Co1B***	***Co2B***	***Co1A***	***Co2A***	***Co1B***	***Co2B***
M1-O1 or M2-O3/Å	1.860(4)	1.862(4)	1.851(4)	1.852(4)	1.860(4)	1.862(4)	1.851(4)	1.852(4)
M1-O2 or M2-O4/Å	1.894(5)	1.898(5)	1.896(5)	1.901(5)	1.894(5)	1.898(5)	1.896(5)	1.901(5)
M1-N1 or M2-N5/Å	1.959(6)	1.942(5)	1.957(6)	1.932(6)	1.959(6)	1.942(5)	1.957(6)	1.932(6)
M1-N2 or M2-N6/Å	1.923(6)	1.893(6)	1.909(5)	1.912(6)	1.923(6)	1.893(6)	1.909(5)	1.912(6)
M1-N3 or M2-N7/Å	1.926(6)	1.897(6)	1.938(6)	1.930(6)	1.926(6)	1.897(6)	1.938(6)	1.930(6)
M1-N4 or M2-N8/Å	1.893(5)	1.920(6)	1.900(6)	1.901(6)	1.893(5)	1.920(6)	1.900(6)	1.901(6)
O1-C1 or O3-C12/Å	1.342(7)	1.353(8)	1.339(7)	1.338(8)	1.342(7)	1.353(8)	1.339(7)	1.338(8)
O2-C2 or O4-C13/Å	1.342(7)	1.329(7)	1.350(7)	1.338(8)	1.342(7)	1.329(7)	1.350(7)	1.338(8)
C1-C2 or C12-C13/Å	1.393(8)	1.398(8)	1.416(9)	1.402(9)	1.393(8)	1.398(8)	1.416(9)	1.402(9)
Diox MOS [a]	–1.8(1)	–2.0(1)	–1.8(2)	–1.91(8)	–1.8(1)	–2.0(1)	–1.8(2)	–1.91(8)
SHAPE (O_h) [b]	0.119	0.197	0.126	0.156	0.119	0.197	0.126	0.156
Σ/deg [c]	29.1	33.7	27.9	29.7	29.1	33.7	27.9	29.7
Θ/deg [c]	73.5	94.0	72.9	83.5	73.5	94.0	72.9	83.5

[a] Dioxolene Metrical Oxidation State as defined by Brown *et al.* ref.[44] [b] *SHAPE* index for octahedral geometry, calculated in *SHAPE* 2.1 and described in text.[46-47] [c] $\Sigma = \sum_{i=1}^{12}|90 - \alpha_i|$ where α_i are the twelve cis-O/N-M-O/N angles about the cobalt atom. $\Theta = \sum_{j=1}^{24}|60 - \theta_j|$ where θ_j are the 24 unique O/N-M-O/N angles, $|\theta_j| < 120°$, measured on the projection of two triangular faces of the octahedron along their common pseudo-threefold axis.[48] Calculated using OctaDist—A program for determining the structural distortion of the octahedral complexes.[49]

Table S8. Variable temperature structural data for **4a**·*x*EtOH

T / K	100	150	200	250	300
Co1-O1/Å	1.917(4)	1.930(7)	1.967(5)	1.997(3)	2.011(3)
Co1-O2/Å	1.971(5)	2.006(9)	2.052(6)	2.083(3)	2.102(3)
Co1-N1/Å	2.013(4)	2.003(7)	2.048(5)	2.075(3)	2.095(3)
Co1-N2/Å	2.072(4)	2.092(7)	2.111(5)	2.130(4)	2.139(3)
Co1-N3/Å	2.089(5)	2.105(7)	2.141(6)	2.173(4)	2.185(4)
Co1-N4/Å	2.117(6)	2.133(9)	2.181(7)	2.223(4)	2.256(4)
O1-C1/Å	1.317(6)	1.32(1)	1.306(8)	1.288(4)	1.278(4)
O2-C2/Å	1.294(8)	1.26(2)	1.27(1)	1.268(5)	1.268(5)
C1-C2/Å	1.445(8)	1.46(1)	1.45(1)	1.456(5)	1.450(5)
Intermolecular Co···Co/Å	7.712(1)	7.700(2)	7.688(1)	7.7018(9)	7.7034(9)
Intramolecular Co···Co′/Å	9.823(2)	9.823(3)	9.838(2)	9.883(1)	9.909(1)
Co1···C11/Å	6.536(5)	6.554(8)	6.576(6)	6.613(3)	6.622(3)
Dihedral angle/° [a]	67.96(9)	69.0(1)	69.5(1)	69.97(7)	70.05(7)
Diox MOS [b]	–1.3(1)	–1.1(2)	–1.14(9)	–1.1(1)	–1.1(1)
SHAPE (O_h) [c]	0.770	0.914	1.069	1.280	1.357
Σ/deg [d]	70.8	77.0	84.4	90.9	94.2
Θ/deg [d]	164.5	180.6	200.9	222.5	230.2

[a] Angle between planes defined by (O1, O2, C1, C2, C3, C4, C5, C6) and intramolecular symmetry equivalent atoms. [b] Dioxolene Metrical Oxidation State as defined by Brown *et al.* ref.[44] [c] *SHAPE* index for octahedral geometry, calculated in *SHAPE* 2.1 and described in text.[46-47] [d] $\Sigma = \sum_{i=1}^{12}|90 - \alpha_i|$ where α_i are the twelve cis-O/N-Co-O/N angles about the cobalt atom. $\Theta = \sum_{j=1}^{24}|60 - \theta_j|$ where θ_j are the 24 unique O/N-Co-O/N angles, $|\theta_j| < 120°$, measured on the projection of two triangular faces of the octahedron along their common pseudo-threefold axis.[48] Calculated using OctaDist—A program for determining the structural distortion of the octahedral complexes.[49]

On heating of **4a**·*x*EtOH from 100 K, the Co···Co and Co···C11 intramolecular distances increase, consistent with both the elongation of the Co-O/N bonds and the DFT optimized structures (Figure S13, Table S8–S9). The dihedral angle between dioxolene planes also increases, but this does not appear to be closely related to the charge distribution as it is not reproduced in DFT optimized structures or correlated with charge distribution in the other spiro and Br_4spiro-bridged dinuclear complexes (Figure S13, Table S8–S10). The overall geometry of $\mathbf{4}^{2+}$ does not change substantially as a result of the VT transition (Figure S14).

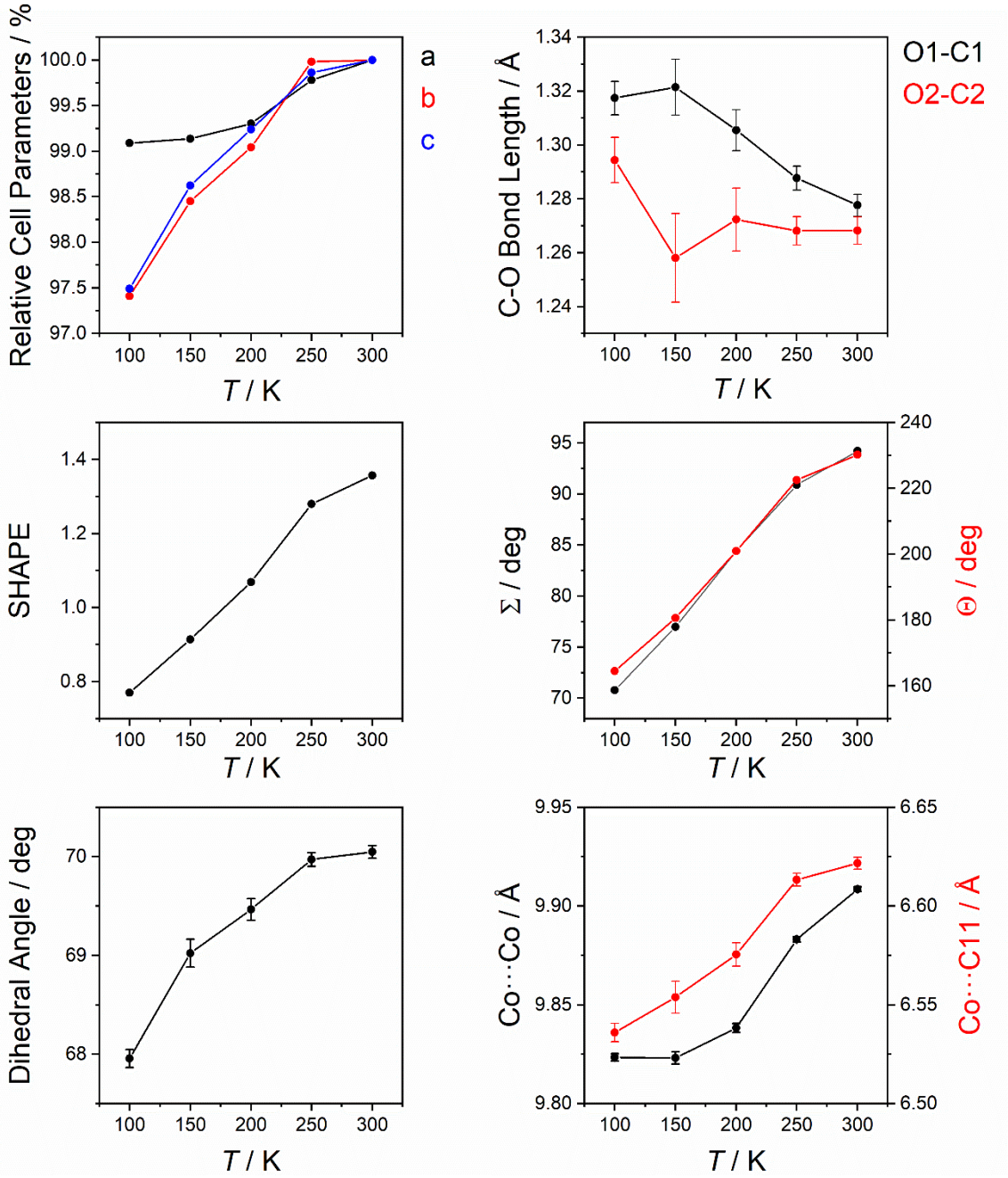

Figure S13. Temperature dependence of various parameters in **4a**·*x*EtOH. Parameters include $a/a_{300\ K}$, $b/b_{300\ K}$ and $c/c_{300\ K}$ cell parameters; C-O bond lengths; octahedral SHAPE, Σ and Θ distortion parameters; dioxolene dihedral angle; Co···Co and Co···C11 intramolecular distances. Error bars are within the data points for relative cell parameters and are not calculated for distortion parameters.

Table S9. Structural data for spiro and Br_4spiro dinuclear compounds (*proximal-proximal* isomers)

Complex	Intramolecular M···M/Å	Intermolecular M···M/Å	M1···C11 /Å	M2···C11 /Å	Dihedral Angle [a] /°	Ref
			Proximal-Proximal Compounds			
pp-**[{Co^{II}(Me$_3$tpa)}$_2$(spiro$^{SQ\text{-}SQ}$)][CoCl$_4$]**·7MeOH	9.497(1)	7.974(1)	6.623(6)	6.578(6)	70.7(1)	38
pp-**[{Co^{III}(tpa)}$_2$(spiro$^{SQ\text{-}SQ}$)](PF$_6$)$_4$**·4acetone	10.465(2)	8.588(2)	6.419(8)	6.477(9)	71.4(2)	38*b*
2a·2.5MeOH	10.075(2)	8.291(2)	6.460(6)	6.460(6)	73.60(8)	
2b$_{pp}$·7acetone, complex ***A***	9.902(3)	8.554(2)	6.482(6)	6.465(6)	66.1(1)	
2b$_{pp}$·3.9acetone, complex ***B***	9.909(2)	8.554(2)	6.457(7)	6.475(7)	65.2(1)	
3a·4.5dioxane	9.731(3)	8.984(2)	6.48(1)	6.48(1)	71.5(2)	
4a·2EtOH, 100 K	9.823(2)	7.712(1)	6.536(5)	6.536(5)	67.96(9)	
4a·2EtOH, 300 K	9.909(1)	7.7034(9)	6.622(3)	6.622(3)	70.05(7)	
5a·2tol	10.307(2)	8.390(2)	6.643(6)	6.631(7)	77.6(1)	
1a {Co^{III}-cat-cat-Co^{III}} DFT	10.203	n/a	6.487	6.482	75.72	
1a {Co^{III}-cat-SQ-Co^{II}} DFT	10.219	n/a	6.644	6.486	74.20	
1a {Co^{II}-SQ-SQ-Co^{II}} DFT	10.204	n/a	6.655	6.658	72.54	
2b$_{pp}$ {Co^{III}-cat-cat-Co^{III}} DFT	10.576	n/a	6.506	6.508	79.53	
2b$_{pp}$ {Co^{III}-cat-SQ-Co^{II}} DFT	10.591	n/a	6.501	6.685	78.46	
2b$_{pp}$ {Co^{II}-SQ-SQ-Co^{II}} DFT	10.600	n/a	6.681	6.684	77.84	
3a {Co^{III}-cat-cat-Co^{III}} DFT	10.578	n/a	6.514	6.514	79.93	
3a {Co^{III}-cat-SQ-Co^{II}} DFT	10.585	n/a	6.509	6.682	78.87	
3a {Co^{II}-SQ-SQ-Co^{II}} DFT	10.636	n/a	6.686	6.688	78.24	
4a {Co^{III}-cat-cat-Co^{III}} DFT	10.669	n/a	6.536	6.536	80.05	
4a {Co^{III}-cat-SQ-Co^{II}} DFT	10.599	n/a	6.532	6.704	78.82	
4a {Co^{II}-SQ-SQ-Co^{II}} DFT	10.620	n/a	6.703	6.703	78.18	

[a] Angle between planes defined by (O1, O2, C1, C2, C3, C4, C5, C6) and intramolecular symmetry equivalent atoms or (O3, O4, C12, C13, C14, C15, C16, C17). [b] A PF_6^- anion is located between the two dioxolene arms of spiro.

Table S10. Structural data for spiro and Br_4spiro dinuclear compounds (*proximal-distal* isomers)

Complex	Intramolecular M···M/Å	Intermolecular M···M/Å	M1···C11 /Å	M2···C11 /Å	Dihedral Angle [a] /°	Ref
***pd*-[{Co^{III}(tpa)}$_2$(spiro$^{cat\text{-}cat}$)] $(PF_6)_2$·4pyridine	9.565(3)	7.736(3)	6.443(9)	6.48(1)	82.1(2)	[38]
2b$_{pd}$·3.9acetone, complex ***A***	10.138(2)	7.345(3)	6.455(6)	6.508(6)	73.4(1)	
2b$_{pd}$·3.9acetone, complex ***B***	10.157(1)	7.345(3)	6.471(6)	6.480(6)	78.5(1)	
6a·tol	9.757(3)	9.474(2)	6.662(4)	6.655(4)	79.57(7)	
2b$_{pd}$ {Co^{III}-cat-cat-Co^{III}} DFT	10.458	n/a	6.505	6.505	78.31	

[a] Angle between planes defined by (O1, O2, C1, C2, C3, C4, C5, C6) and intramolecular symmetry equivalent atoms or (O3, O4, C12, C13, C14, C15, C16, C17). [b] A PF_6^- anion is located between the two dioxolene arms of spiro.

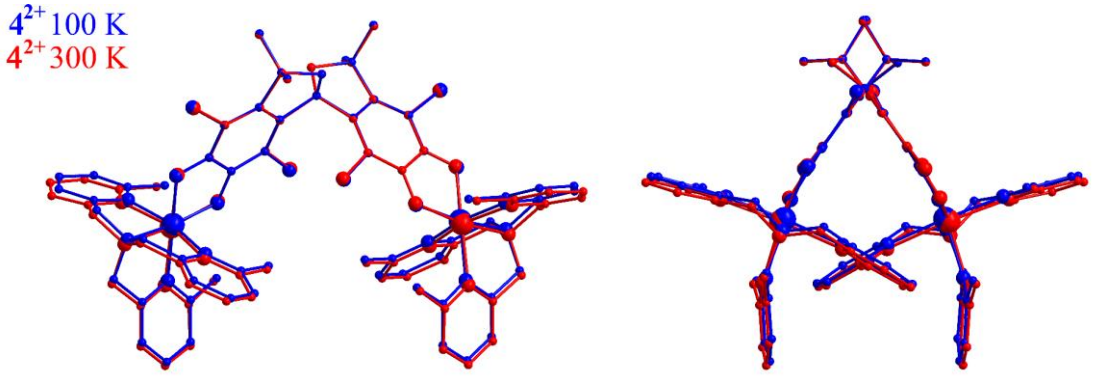

Figure S14. Overlaid structure of $\mathbf{4}^{2+}$ in **4a**·2EtOH at 100 K (blue) and 300 K (red) viewed from two different angles.

Magnetic Data

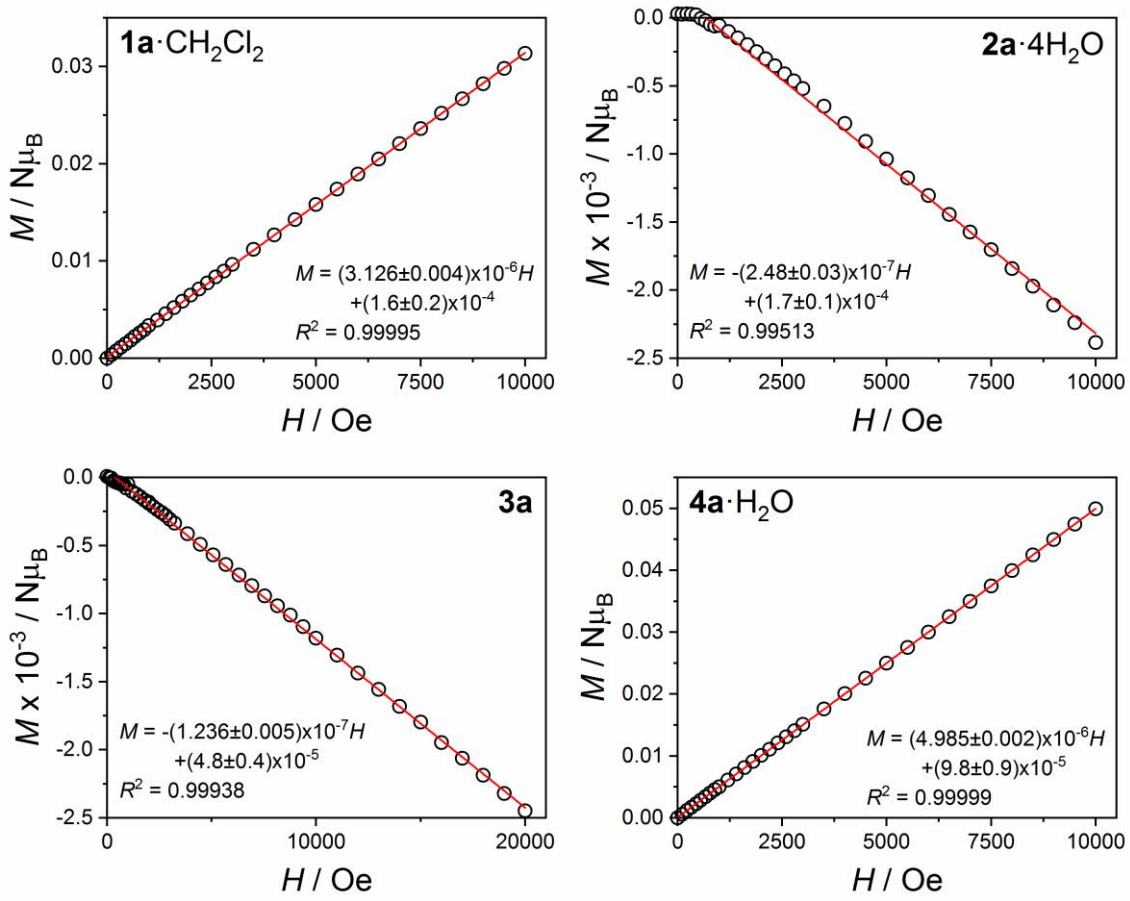

Figure S15. Ferromagnetic check for impurities at 100 K for **1a**·CH_2Cl_2, **2a**·$4H_2O$, **3a** and **4a**·H_2O.

Inset: R^2 value for a linear fit, a linear response indicates no impurities.

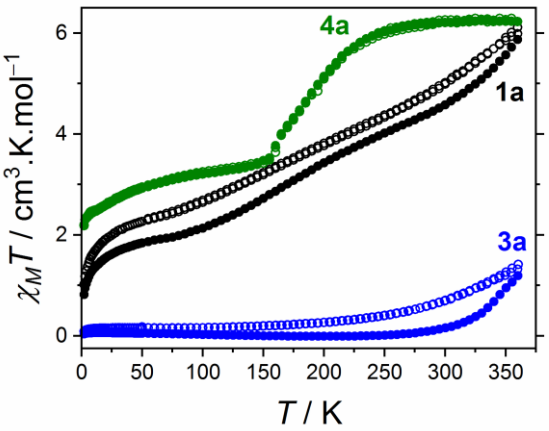

Figure S16. Plots of $\chi_M T$ vs T for **1a**·CH_2Cl_2 (black), **3a** (blue) and **4a**·H_2O (green) on first heating (filled circles) and on a repeated cooling and heating cycle (empty circles).

UV-visible Spectroscopy

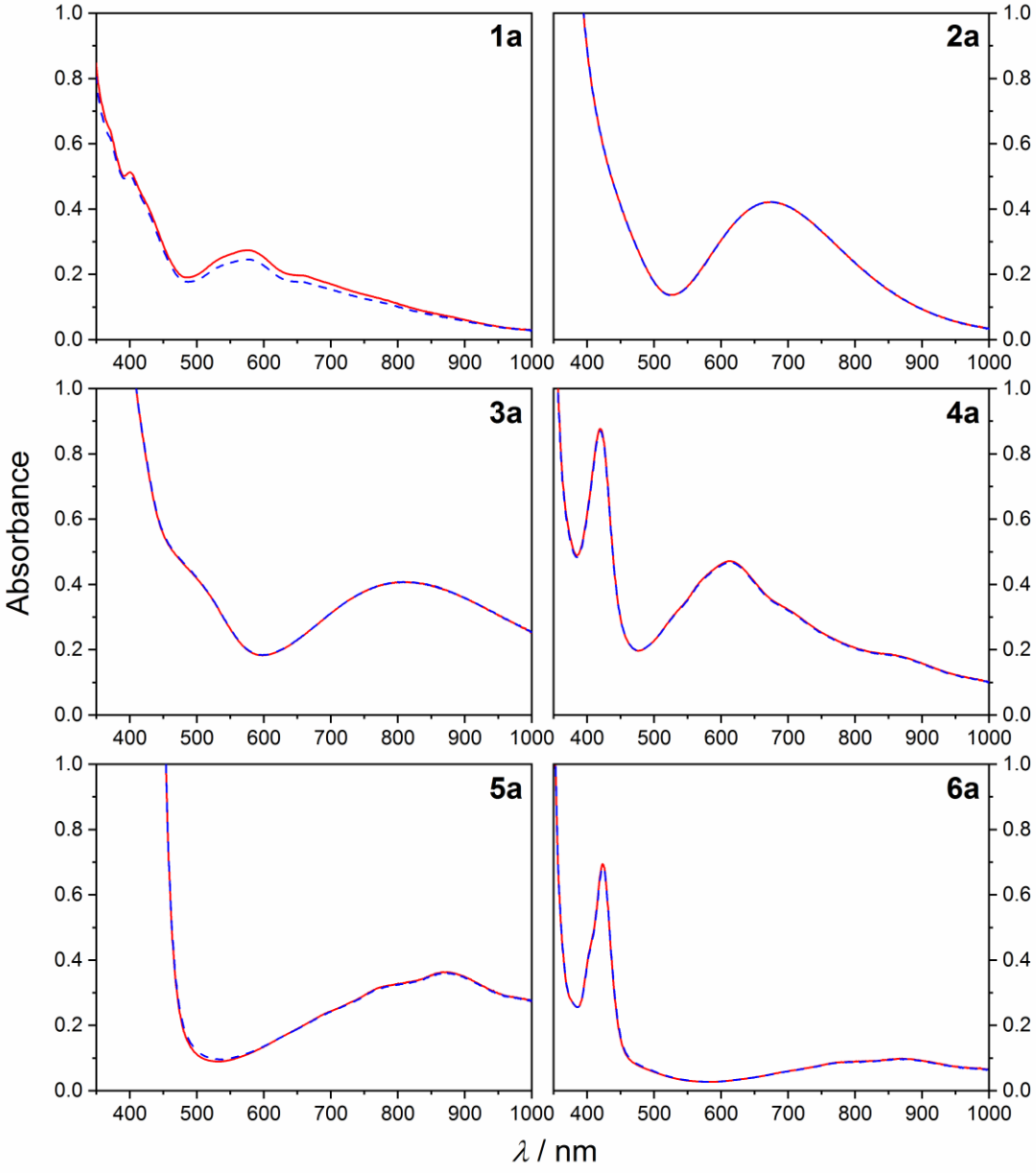

Figure S17. UV-vis absorption spectra of MeCN solutions of **1a**–**6a** in air – immediately following dissolution (red solid line) and after 1.5 h (**1a**) or 4–5 h (**2a**–**6a**, blue dashed line).

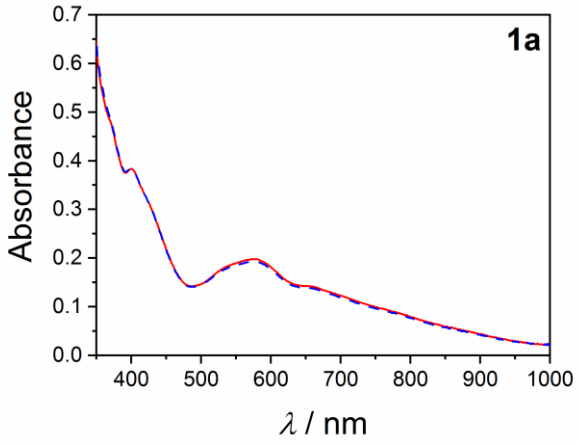

Figure S18. UV-vis absorption spectrum of an acetonitrile solution of **1a** under nitrogen – immediately following dissolution (red solid line) and after 4 h (blue dashed line).

Table S11. Electronic absorption bands for acetonitrile solutions of Br$_4$spiro compounds **2a**–**6a**.

Assignment	λ/nm (ε/mol L^{-1} cm^{-1})			Ref
	2a	**3a**		
Me$_n$tpa LC: $\pi^* \leftarrow \pi$	473 (353sh)	388 (1,770sh)		[50]
	-	535 (397sh)		[50]
LMCT	674 (516)	809 (515)		[40,50-51]
	4a	**5a**	**6a**	
SQ LC: $3b_1 \leftarrow 9a_1$ ($\pi^* \leftarrow$ n)	420 (5,370)	416 (2,580sh)	405 (3,380sh)	[51]
	-	433 (3,480)	423 (5,290)	[51]
$^4T_1(P) \leftarrow {}^4T_1(F)$ [a]	538 (1,990sh)	-	-	[52-53]
MLCT	614 (2,910)	-	-	[3,54]
SQ LC: $3b_1 \leftarrow 2a_2$ ($\pi^* \leftarrow \pi$) [b]	695 (2,020sh)	702 (309sh)	716 (525sh)	[51]
	-	803 (414sh)	800 (718sh)	[51]
	844 (1,130sh)	872 (456)	870 (777)	[51]
	972 (674sh)	974 (360sh)	978 (539sh)	[51]
IVCT	-	1494 (136) [c]	-	[55]

Abbreviations: LC = ligand-centered, LMCT = ligand-to-metal charge transfer, MLCT = metal-to-ligand charge transfer, IVCT = inter-valence charge transfer. [a] Assigned based on the absence of a band in $\mathbf{5}^+$ and $\mathbf{6}^{2+}$. [b] Band is split due to vibronic coupling with the C-O stretching mode.[51] [c] Maximum as determined from ε versus λ. The fitted maximum of (ε/ν) versus ν occurs at 5631 cm^{-1} (1776 nm).

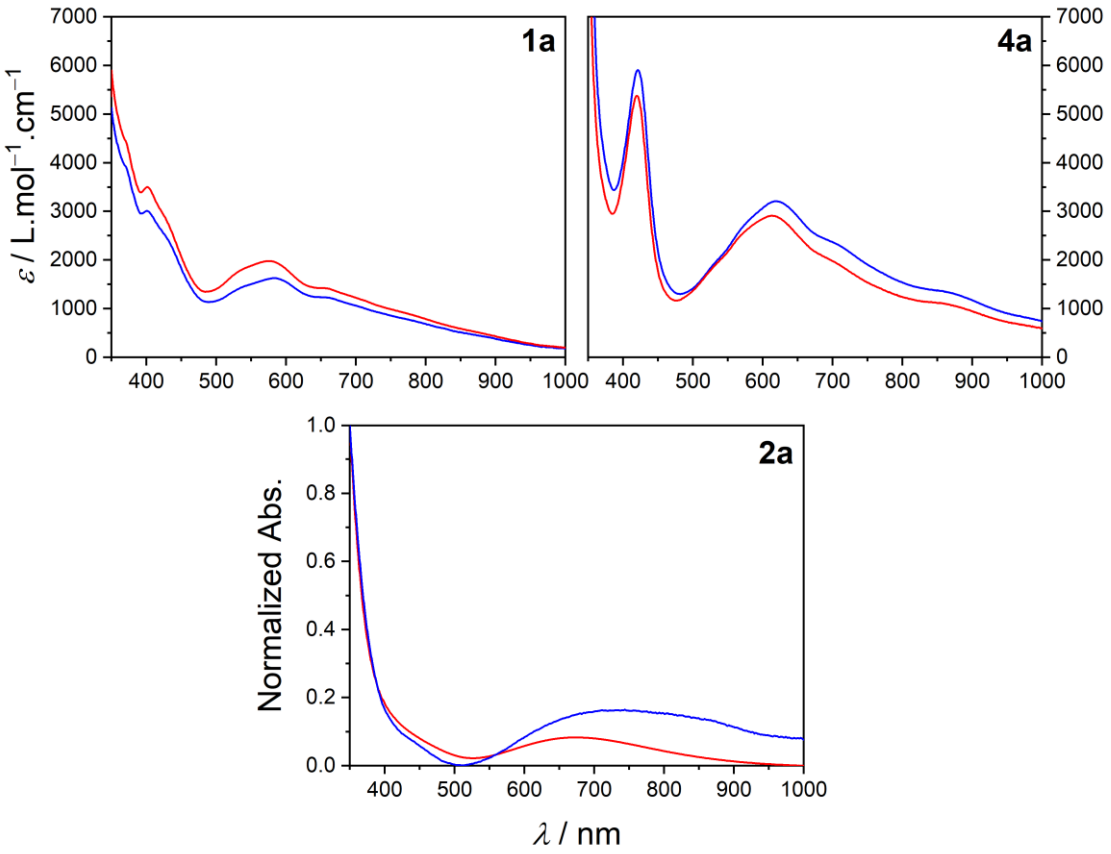

Figure S19. UV-vis absorption spectra of acetonitrile (red) and tetrahydrofuran (blue) solutions of **1a**, **2a** and **4a**. Presented as normalized absorbance for **2a** due to poor solubility of **2a** in tetrahydrofuran resulting in significant scattering and uncertainty in the concentration.

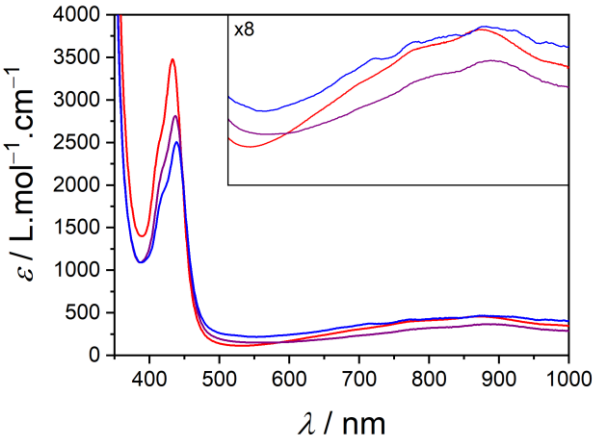

Figure S20. UV-vis absorption spectra of **5a** in acetonitrile (red), 1,2-dichloroethane (purple) and chlorobenzene (blue).

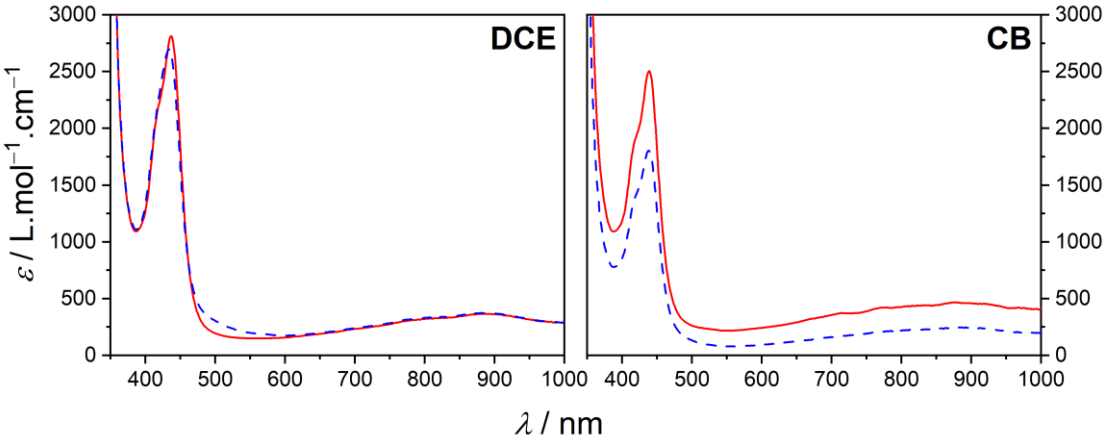

Figure S21. UV-vis absorption spectra of 1,2-dichloroethane (DCE) and chlorobenzene (CB) solutions of **5a** in air – immediately following dissolution (red solid line) and after 5 h (blue dashed line).

NIR Spectroscopy and Mixed-Valence Analysis

The electronic structure of Robin-Day mixed-valence (MV) class I, II and III complexes are given in Figure S22.[56-57] Class I corresponds to localized electronic structures with no interaction of the two centers, where the electronic coupling parameter, H_{AB}, is equal to zero. Class II corresponds to localized electronic structures and localized solvent interactions, which result in an inter-valence charge transfer (IVCT) band of energy $h\nu_{max}$ and full width at half maximum, $\Delta\nu_{1/2}$. The values of ν_{max} (cm^{-1}) and $\Delta\nu_{1/2}$ (cm^{-1}) are obtained by fitting a Gaussian curve to the IVCT band when plotted as (ε/ν) versus ν, as appropriate for wavelength-dependent charge transfers.[58] The IVCT for class II is typically solvent-dependent ($\Delta\nu_{max} \geq 200$ cm^{-1} over a range of dielectric constant of 30),[58-59] weak in intensity ($\varepsilon_{max} \leq 5000$ L mol^{-1} cm^{-1}), broad ($\Delta\nu_{1/2} \geq 2000$ cm^{-1}) and has $2H_{AB}/\nu_{max} \ll 1$.[58] Class II-III corresponds to localized electronic structures and averaged solvent interactions, given relative rates of bond vibrations and solvent reorientations, class II-III complexes are expected to have $0.7 < 2H_{AB}/\nu_{max} < 1$.[58] Class III corresponds to electronic and solvent delocalization with $2H_{AB}/\nu_{max} \gg 1$. Both MV class II-III and MV class III complexes are expected to have narrow ($\Delta\nu_{1/2} \leq 2000$ cm^{-1}), intense ($\varepsilon_{max} \geq 5000$ L mol^{-1} cm^{-1}) and solvent-independent electronic transitions ($\Delta\nu_{max} \leq 200$ cm^{-1} over a range of dielectric constant of 30).[59]

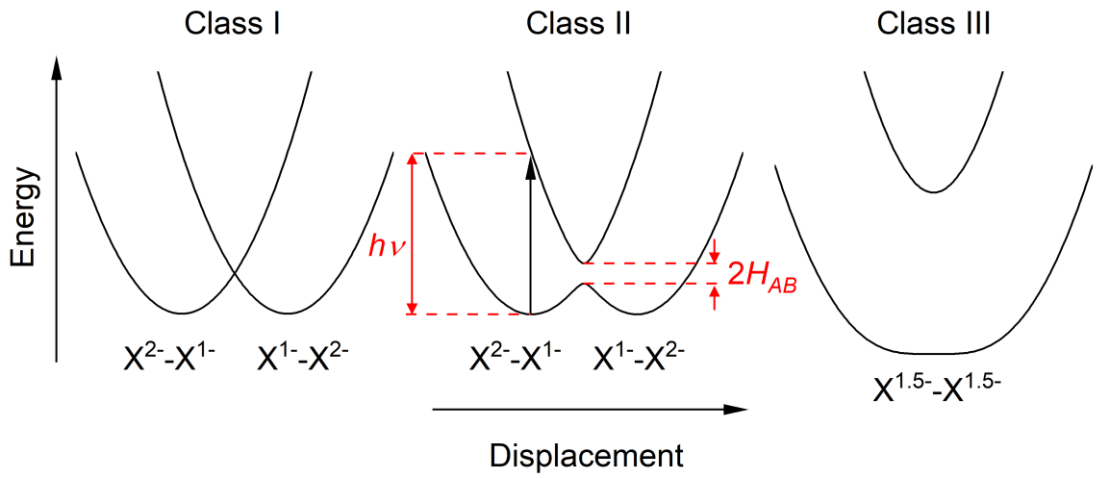

Figure S22. Robin-Day classification of mixed-valence compounds showing the energy of the inter-valence charge transfer (IVCT) transition and the electronic coupling parameter, H_{AB}. Here X represents a dioxolene moiety that can be in the cat^{2-} or SQ^{1-} redox form.[56-57]

The MV class can also be determined by the parameter Γ, as given by Equation S1:

$$\Gamma = 1 - (\Delta\nu_{1/2})/(\Delta\nu_{1/2}°) \qquad \text{(Eq. S1)}$$

where $\Delta\nu_{1/2}°$ is the theoretical bandwidth at half maximum of the IVCT (cm^{-1}) as given by Equation S2:

$$\Delta\nu_{1/2}° = (16RT(\ln 2)\nu_{max})^{1/2} = (2310\nu_{max})^{1/2} \text{ at 298 K.} \qquad \text{(Eq. S2)}$$

Values of $\Gamma < 0.5$ indicate class II, values of $\Gamma \approx 0.5$ indicate class II-III and values of $\Gamma > 0.5$ indicate class III. For organic/redox-active ligand MV substances, H_{AB} takes values of up to ~800

cm^{-1} for MV class II (typically 350–800 cm^{-1}),[60-61] ~1000–2000 cm^{-1} for class II-III [55,62] and 2500–5500 cm^{-1} for class III.[60-61]

According to the Hush model,[56,63-64] H_{AB}, may be calculated according to Equation 3:

$$H_{AB1} = \frac{2.06\times10^{-2}(\nu_{max}\varepsilon_{max}\Delta\nu_{1/2})^{1/2}}{r_{AB}} \quad \text{(Eq. S3)}$$

where ε_{max} (L mol^{-1} cm^{-1}) is the molar absorptivity at maximum (ε/ν) and r_{AB} is the distance (Å) between the two centers, approximated for $\mathbf{5}^{+}$ as the distance between the centroids of O1-C1-C2-O2 and O3-C12-C13-O4 in **5a**·2tol (r_{AB} = 7.58 Å).[60]

The Brunchwig-Sutin model[65] provides an alternative measure of H_{AB}, which uses complementary electrochemistry data to calculate the comproportionation equilibrium constant (K_c) for the reaction: $\{SQ\text{-}SQ\}^{2+} + \{cat\text{-}cat\}^{0} \rightleftharpoons 2\{cat\text{-}SQ\}$:

$$\Delta G_c^{\circ} = -RT \ln K_c = -F(\Delta diox) \quad \text{(Eq. S4)}$$

where ΔG_c° is the Gibbs free energy of the comproportionation reaction (J mol^{-1}), F is Faraday's constant which takes the value 95485 C mol^{-1}, and $\Delta diox$ is the separation (V) between successive redox processes **I** and **II** as detailed in the main text. For partially delocalized complexes, H_{AB} is given by Equation S5:[65]

$$H_{AB2} = \left(\frac{-\Delta G_r^{\circ}\nu_{max}}{2}\right)^{1/2} \approx \left(\frac{-\Delta G_c^{\circ}\nu_{max}}{2}\right)^{1/2} \quad \text{(Eq. S5)}$$

where $\Delta G_c°$ is the Gibbs free energy of the comproportionation reaction (cm^{-1}), which can be approximated as the Gibbs free energy due to the electronic interaction by delocalization, $\Delta G_r°$, in the case of small non-resonance contributions. In the case of fully delocalized complexes, Equation S6 should be used instead:[65]

$$H_{AB2} = -\frac{\Delta G_r°}{2} + \frac{\nu_{max}}{4} \approx -\frac{\Delta G_c°}{2} + \frac{\nu_{max}}{4} \quad \text{(Eq. S6)}$$

Values above the upper limit of H_{AB} (Equation S7) correspond to MV class III complexes.

$$H_{AB3} = \frac{\nu_{max}}{2} \quad \text{(Eq. S7)}$$

Near infrared spectra were recorded for **5a** in acetonitrile (dielectric constant, κ = 37.5), 1,2-dichloroethane (κ = 10.36) and chlorobenzene (κ = 5.62), and are given in Figure 5 and Figure S23. The NIR data in 1,2-dichloroethane and acetonitrile were plotted as the reduced spectrum, (ε/ν) versus ν, and Gaussian curves were fit to extract ν_{max} and $\Delta\nu_{1/2}$ (Table S12). In Table S12 are given the resulting values of Γ (Equation S1), $\Delta\nu_{1/2}°$ (Equation S2), H_{AB1} from the Hush model (Equation S3), H_{AB2} from the Brunchwig-Sutin model (Equation S5–S6), the limiting value H_{AB3} (Equation S7) and the ratio $2H_{AB}/\nu_{max}$. No clear peak was observed in the reduced NIR spectrum of **5a** in chlorobenzene (Figure S23) and fitting was unsuccessful; **5a** was also unstable over time in chlorobenzene (Figure S21). Mixed-valence and electrochemical parameters of literature bis(dioxolene) complexes are given in Table S13.

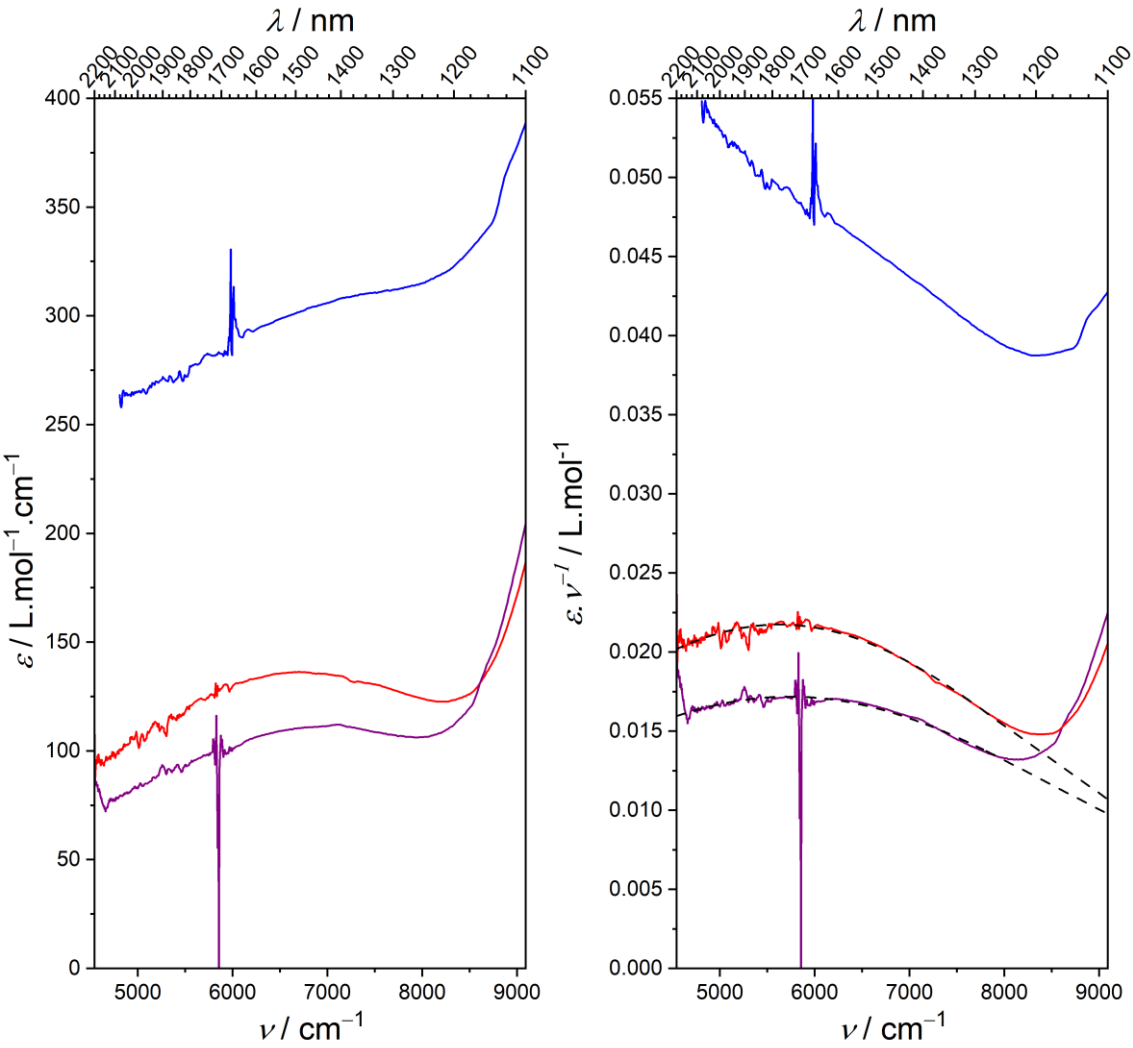

Figure S23. Near infrared absorption spectra of **5a** dissolved in acetonitrile (red), 1,2-dichloroethane (purple) and chlorobenzene (blue) showing ε (left) and ε/ν (right) with Gaussian fits (black dashed). Parameters given in Table S12.

Table S12. Mixed-valence and IVCT parameters for complex **5a** [a]

Solvent	ν_{max}/cm^{-1}	$\Delta\nu_{1/2}$/cm^{-1}	$(\varepsilon/\nu)_{max}$/L mol cm^{-2}	$\Delta\nu_{1/2}°$/cm^{-1}	Γ	$\Delta diox$/mV
1,2-Dichloroethane	5737(8)	7310(50)	0.01718(1)	3640	−1.01	n/a [b]
Acetonitrile	5631(8)	6670(40)	0.02173(2)	3607	–0.85	175
Solvent	$\Delta G_c°$/kJ mol^{-1}	H_{AB1}/cm^{-1}	$(2H_{AB1}/\nu_{max})$	H_{AB2}/cm^{-1} [c]	$(2H_{AB2}/\nu_{max})$ [c]	H_{AB3}/cm^{-1} [c]
1,2-Dichloroethane	n/a [b]	175	0.06	n/a [b]	n/a [b]	2870
Acetonitrile	−16.9	184	0.07	1990 (2110)	0.71 (0.75)	2820

[a] From Gaussian fit of ε/ν versus ν in the range of 7900 cm^{-1} to the low energy solvent absorption limit. Experimental noise from 5790–5890 cm^{-1} was excluded when fitting 1,2-dichloroethane data. Chlorobenzene data could not be fit. Parameters calculated using Equations S1–S7. [b] Electrochemical data not measured in 1,2-dichloroethane. [c] Value given using partially delocalized formula in Equation S5, value in brackets is calculated using Equation S6 for a fully delocalized complex.

Table S13. Electronic coupling parameters for selected bis(dioxolene) ligands in Chart S2 [a]

Bis(dioxolene)	**M**$^{\text{O.S.}}$	**Ancillary ligand(s)**	**$\Delta diox$ /mV**	**H_{AB1} /cm^{-1}**	**H_{AB2}** [b] **/cm^{-1}**	**H_{AB3} limit** [c] **/cm^{-1}**	**$2H_{AB1}/\nu_{max}$**	**$2H_{AB2}/\nu_{max}$**	**Γ** [b]	**MV Class**	**Ref**
m-Ph(cat)$_2$ [d]	Pd^{II}	*t*Bu$_2$bpy	82	0	0	-	-	-	-	I	60
p-Ph(cat)$_2$	Pd^{II}	*t*Bu$_2$bpy	119	670	1770 (2130)	-	>0.20	0.54 (0.64)	–0.30	II	60
thea	Pt^{II}	dppb	230	280 [e,f]	2250 (2300)	2760	>0.10 [e,f]	0.81 (0.83)	0.36	II-III	55
thea	Pt^{II}	dppe	270	550 [f]	2440 (2460)	2760	>0.20 [f]	0.88 (0.89)	0.36	II-III	55
bis(catechol)	Pd^{II}	*t*Bu$_2$bpy	365	1530	3290 (3310)	3710	>0.41	0.89 (0.89)	0.52	II-III	60
hhad [g]	Ru^{II}	(PBu$_3$)$_2$(CO)$_2$	440	- [h]	2550 (2680)	1860	- [h]	1.38 (1.45)	0.32	II-III	62
tmdmp	Pd^{II}	*t*Bu$_2$bpy	280 [i]	1290	3510 (3870)	5500	>0.23	0.64 (0.70) [i]	0.81	III	60

Abbreviations: *m*-Ph(catH$_2$)$_2$ = 1,3-bis(3′,4′-dihydroxyphenyl)benzene; *t*Bu$_2$bpy = 4,4′-bis(*tert*-butyl)-2,2′-bipyridyl; *p*-Ph(catH$_2$)$_2$ = 1,4-bis(3′,4′-dihydroxyphenyl)benzene; theaH$_4$ = 2,3,6,7-tetrahydroxy-9,10-dimethyl-9,10-dihydro-9,10-ethanoanthracene; dppb = 1,2-bis(diphenylphosphino)benzene; dppe = 1,2-bis(diphenylphosphino)ethane; bis(catechol) = 3,3′,4,4′-tetrahydroxybiphenyl; hhadH$_4$ = 1,2,3,5,6,7-hexahydroxyanthracene-9,10-dione; tmdmpH$_4$ = 2,3,6,7-tetramethoxy-9,10-dimethylphenanthrene. [a] Measurements performed in dichloromethane (κ = 8.93). Parameters calculated using Equations S1-S7. [b] Value given using partially delocalized formula in Equation S5, value in brackets is calculated using Equation S6 for a fully delocalized complex. [c] H_{AB3} is valid for MV class III systems and is given for MV class II-III and MV class III systems only. [d] No IVCT observed for this complex. [e] r_{AB} calculated from one-electron reduced structure. [f] Band has not been fit to a Gaussian curve and $\Delta\nu_{1/2}$ has been approximated. [g] Metal binds at 2,3 and 6,7 positions of hhad. [h] Absence of a crystal structure precluded determination of r_{AB} and H_{AB}. [i] Potential of second oxidation wave is split due to the formation of a dimer on the electrode surface, so the potential has been approximated.

Chart S2. Bis(dioxolene) proligands employed in compounds described in Table S13.[55,60,62]

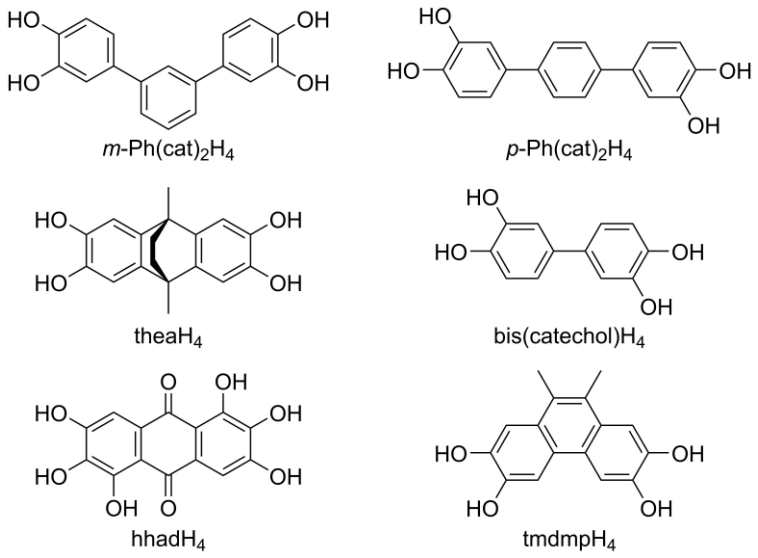

The observation of localized cat^{2-} and $SQ^{\bullet-}$ bands on the IR timescale for **5a** (Table S4) indicates electronic localization and rules out MV class III. The broadness and low intensity of the IVCT in **5a** suggests MV class II character, which is supported by $\Gamma < 0.5$. The Γ parameter appears to be an accurate measure of MV class for bis(dioxolene) complexes (Table S13), although there is an error associated with fitting the IVCT of **5a** when the low and high energy tails are obscured by solvent absorption and other electronic transitions, respectively. A value of $2H_{AB1}/\nu_{max}$ of 0.06–0.07 also suggests MV class II for **5a**. However, H_{AB1} (175–184 mV) is considered a lower limit of H_{AB} as r_{AB} is underestimated by the geometric distance, and $2H_{AB1}/\nu_{max}$ is a poor indication of MV class in literature bis(dioxolene) complexes (Table S13). The value of $2H_{AB2}/\nu_{max}$ shows a stronger correlation with MV class in literature bis(dioxolene) complexes. For complex **5a**, $2H_{AB2}/\nu_{max}$ = 0.71–0.75 is on the border of class II and class II-III. The decisive feature is the weak solvent dependence of the IVCT (Figure S23, Table S12, $\Delta\nu_{max}$ = 110(20) cm^{-1}) which confirms MV class II-III character for **5a**.[59]

Electrochemistry

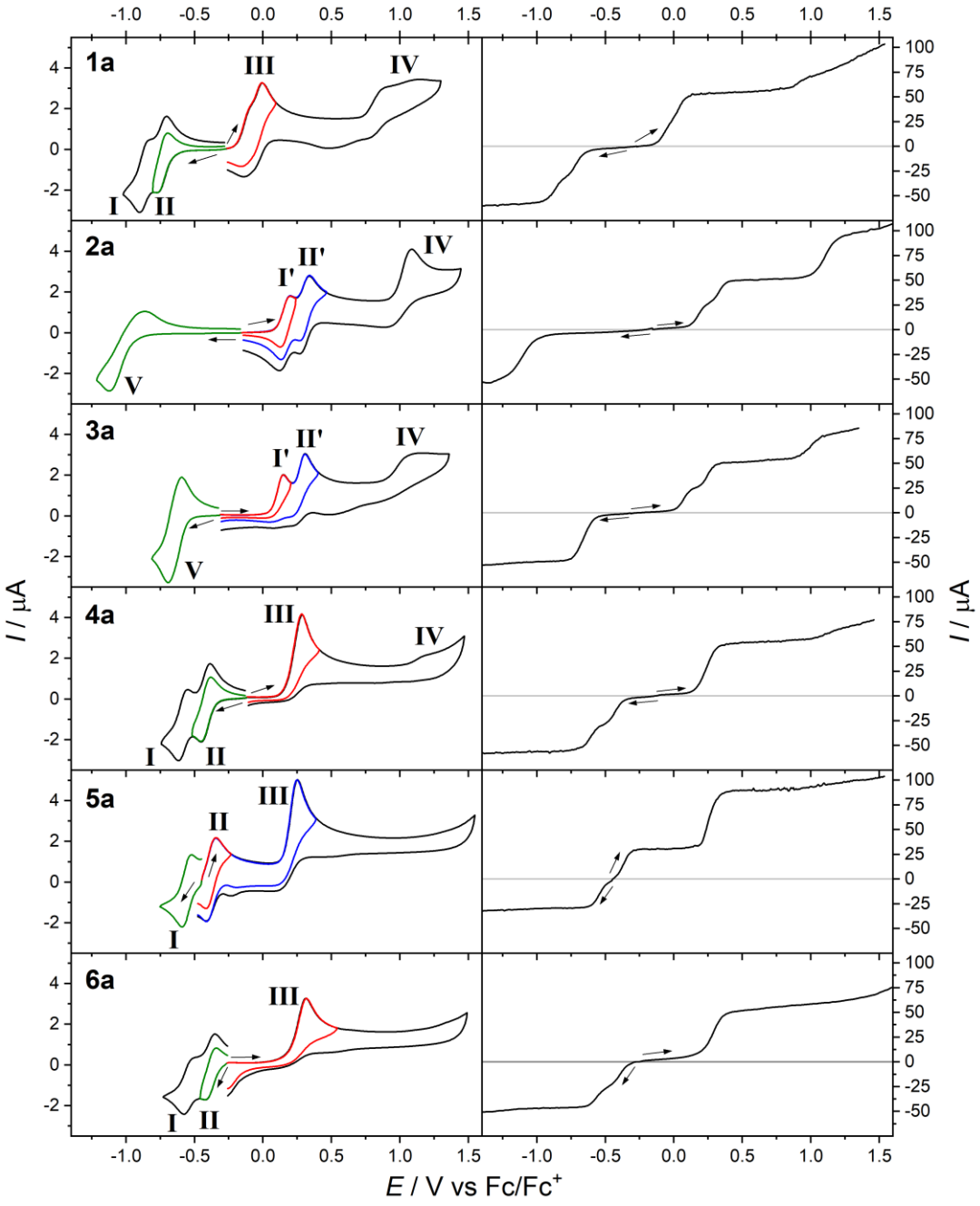

Figure S24. (*Left*) Cyclic voltammograms of MeCN solutions of compounds **1a**–**6a** (1.0 mM with 0.25 M Bu_4NPF_6) at a scan rate of 100 mV s^{-1}. The colored lines plot the voltammograms measured with a switching potential immediately past the first oxidation (red), second oxidation (blue) and first reduction (green). (*Right*) Corresponding RDE voltammograms obtained at a scan rate of 50 mV s^{-1} and a rotation rate of 500 rotations min^{-1}. Arrows indicate the direction of the scan.

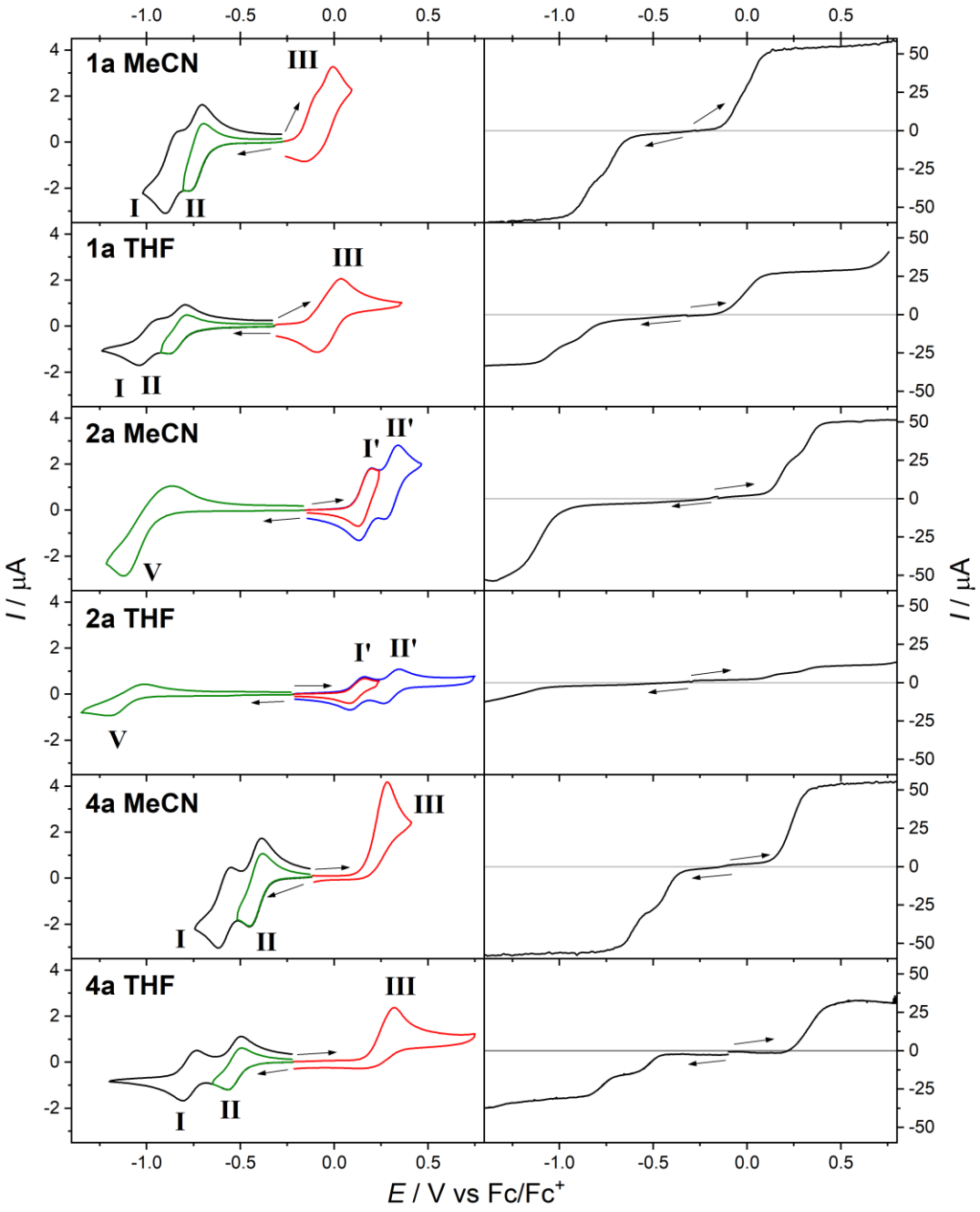

Figure S25. (*Left*) Cyclic voltammograms of acetonitrile and tetrahydrofuran solutions of compounds **1a**, **2a** and **4a** (1.0 mM with 0.25 M Bu_4NPF_6) at a scan rate of 100 mV s^{-1}. The colored lines plot the voltammograms measured with a switching potential immediately past the first oxidation (red), second oxidation (blue) and first reduction (green). (*Right*) Corresponding RDE voltammograms obtained at a scan rate of 50 mV s^{-1} and a rotation rate of 500 rotations min^{-1}. Arrows indicate the direction of the scan. Note that compound **2a** had limited solubility in tetrahydrofuran and precipitation was observed in the cell.

Table S14. Cyclic voltammetry and rotating disk electrode voltammetry data for compounds **1a**, **2a** and **4a** in tetrahydrofuran [a]

	Cyclic Voltammetry Data				Rotating Disk Electrode Voltammetry			
	E_m or E_p/V (ΔE_p/mV)				$E_{1/2}$ / V (i_L/μA)			
	I/I′	**II/II′**	**III**	**V**	**I/I′**	**II/II′**	**III**	**V**
1a	–0.978 (126)	–0.838 (89)	–0.028 (129)	n/a	–1.041 (13.5)	–0.857 (13.6)	–0.067 (26.4)	n/a
2a	0.123 (79)	0.304 (83)	n/a	–1.109 (192)	0.124 (4.0)	0.314 (4.0)	n/a	–1.186 (7.8)
4a	–0.770 (74)	–0.532 (72)	0.320 [b]	n/a	–0.772 (13.5)	–0.525 (12.8)	0.333 (34.4)	n/a

[a] 1.0 mM in tetrahydrofuran with 0.25 M Bu_4NPF_6. Compound **2a** showed limited solubility, reflected in the smaller i_L values. Potentials reported versus Fc/Fc^+ couple. Error in potentials is ±5 mV. [b] E_p rather than E_m.

Process **IV** is observed at high potentials for **1a**–**4a** in MeCN (Figure 6) and did not lie within the accessible potential window in THF (Figure S25). The RDE voltammogram of process **IV** is only well-defined for **2a**, which suggests a 2e-oxidation of the $\{Co^{III}\text{-SQ-SQ-}Co^{III}\}^{4+}$ species to $\{Co^{III}\text{-Q-Q-}Co^{III}\}^{6+}$ (Q = quinone). For complex **2a**, the $\{Co^{III}\text{-SQ-SQ-}Co^{III}\}^{4+}$ species generated by oxidation **II′** is stable, leading to a well-defined oxidation **IV**. The $\{Co^{III}\text{-SQ-SQ-}Co^{III}\}^{4+}$ species generated by oxidation **II′** is less stable for complex **3a**, resulting in a smaller peak current for process **IV**.

As mentioned in the main text, the $\{Co^{II}\text{-Q-Q-}Co^{II}\}^{4+}$ species formed by process **III** is thought to dissociate. However, the presence of process **IV** in the voltammetry for cobalt compounds **1a** and **4a** suggests that the $\{Co^{II}\text{-Q-Q-}Co^{II}\}^{4+}$ species formed following oxidation through process **III** undergoes a partial charge redistribution to the more thermodynamically-stable isoelectronic species, $\{Co^{III}\text{-SQ-SQ-}Co^{III}\}^{4+}$ (Scheme 1, Table S15, Figure S28). This interconversion is not possible for zinc compounds **5a** and **6a**, and so process **IV** is not observed. The extent of charge redistribution of the tetracationic species depends on competition with

dissociation of the dinuclear complex, but enough of the $\{Co^{III}\text{-SQ-SQ-}Co^{III}\}^{4+}$ complex exists in the voltammetry experiments to enable observation of process **IV** for **1a** and **4a**, albeit with a small current and poorly defined RDE processes.

Computational Investigation of Electrochemical Assignments

To confirm the assignment of the electrochemical processes, geometry optimizations were performed on complex $\mathbf{2_{pp}}^{2+}$ in the ground state and reduced and optimized forms. As the HOMO of {Co^{III}-cat-cat-Co^{III}} is ligand-centered (Figure S26), the first oxidation is expected to be ligand-based. Indeed, removing an electron from $\mathbf{2_{pp}}^{2+}$ (process **I**) results in the formation of a {Co^{III}-cat-SQ-Co^{III}} species, $\mathbf{2_{pp}}^{3+}$, characterized by the absence of spin density on cobalt and delocalization of one electron over the ligand system (Figure S27). The ligand bond lengths are intermediate between those typical for the catecholate and semiquinonate forms. A second one-electron oxidation (process **II**) results in the formation of $\mathbf{2_{pp}}^{4+}$ with the charge distribution {Co^{III}-SQ-SQ-Co^{III}}. The charge distribution is confirmed by the bond lengths and the spin density on the semiquinone fragments, which is twice as large as in $\mathbf{2_{pp}}^{3+}$ (Figure S27). The last two-electron oxidation (process I**V**) stabilizes the diamagnetic {Co^{III}-Q-Q-Co^{III}} species with bond lengths characteristic of the neutral quinone form of the dioxolene (Figure S27). A two-electron reduction (process **V**) of $\mathbf{2_{pp}}^{2+}$ stabilizes {Co^{II}-cat-cat-Co^{II}} state, $\mathbf{2_{pp}}$. The assignment of process **V** is confirmed by almost unchanged dioxolene C-C bond lengths and spin density localized on the cobalt centers (Figure S26). Thus, an analysis of the spin density distribution and the calculated bond lengths confirm the assignment of the electrochemical processes made in Scheme 1: in the $\mathbf{2_{pp}}^{2+}$ complex, processes **I** and **II** are the ligand-centered oxidations, while the reduction process **V** occurs at the metal ions.

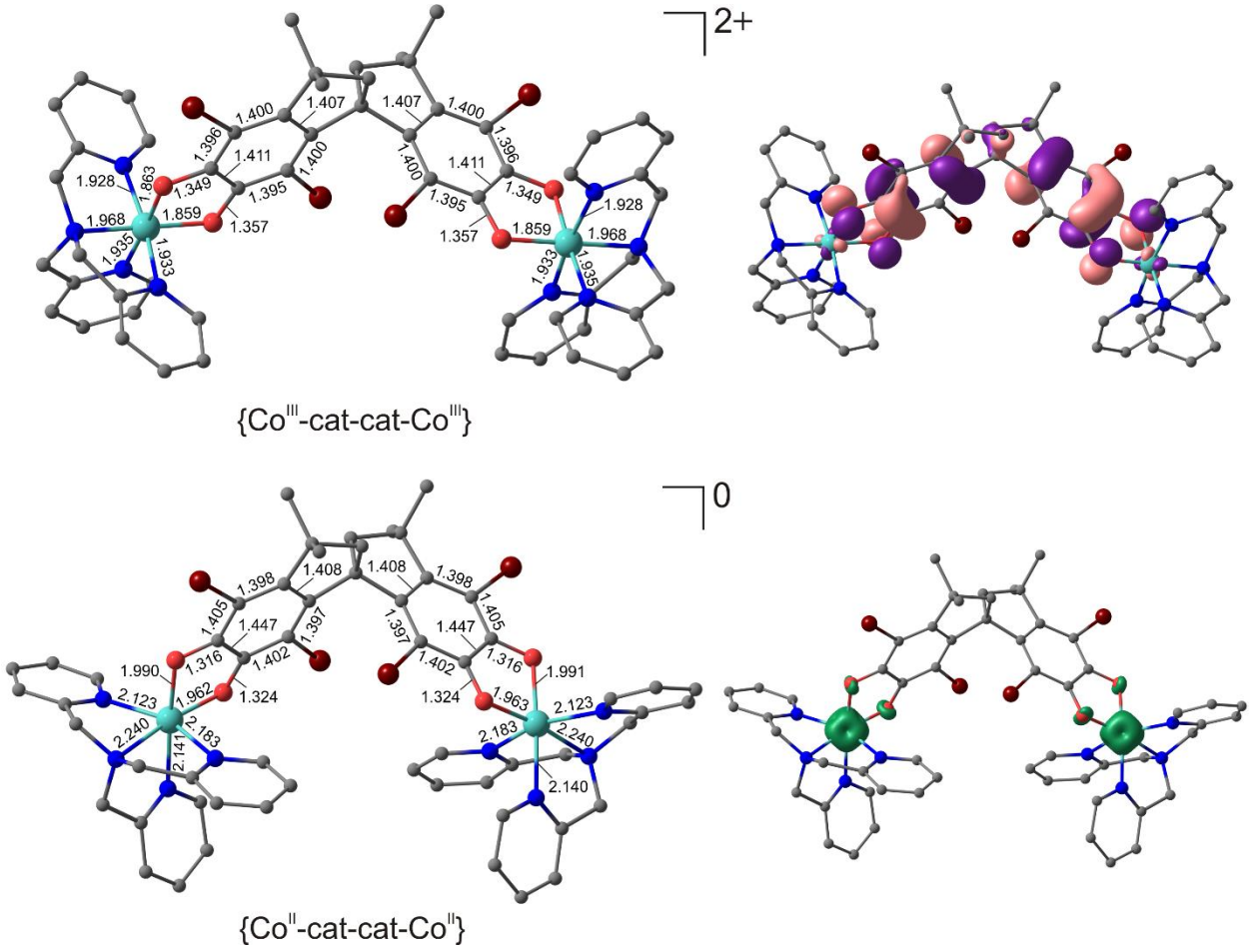

Figure S26. Optimized geometries (*left*) of the initial and reduced species of $\mathbf{2_{pp}}^{2+}$ as calculated by the DFT UTPSSh/6-311++G(d,p) method. Corresponding HOMO (cutoff = 0.036 e/Å^3) of the {Co^{III}-cat-cat-Co^{III}} charge distribution (*right*) and spin density distribution (cutoff = 0.015 e/Å^3) of the {Co^{II}-cat-cat-Co^{II}} charge distribution (*right*). Hereinafter hydrogen atoms are omitted; bond lengths are given in Å.

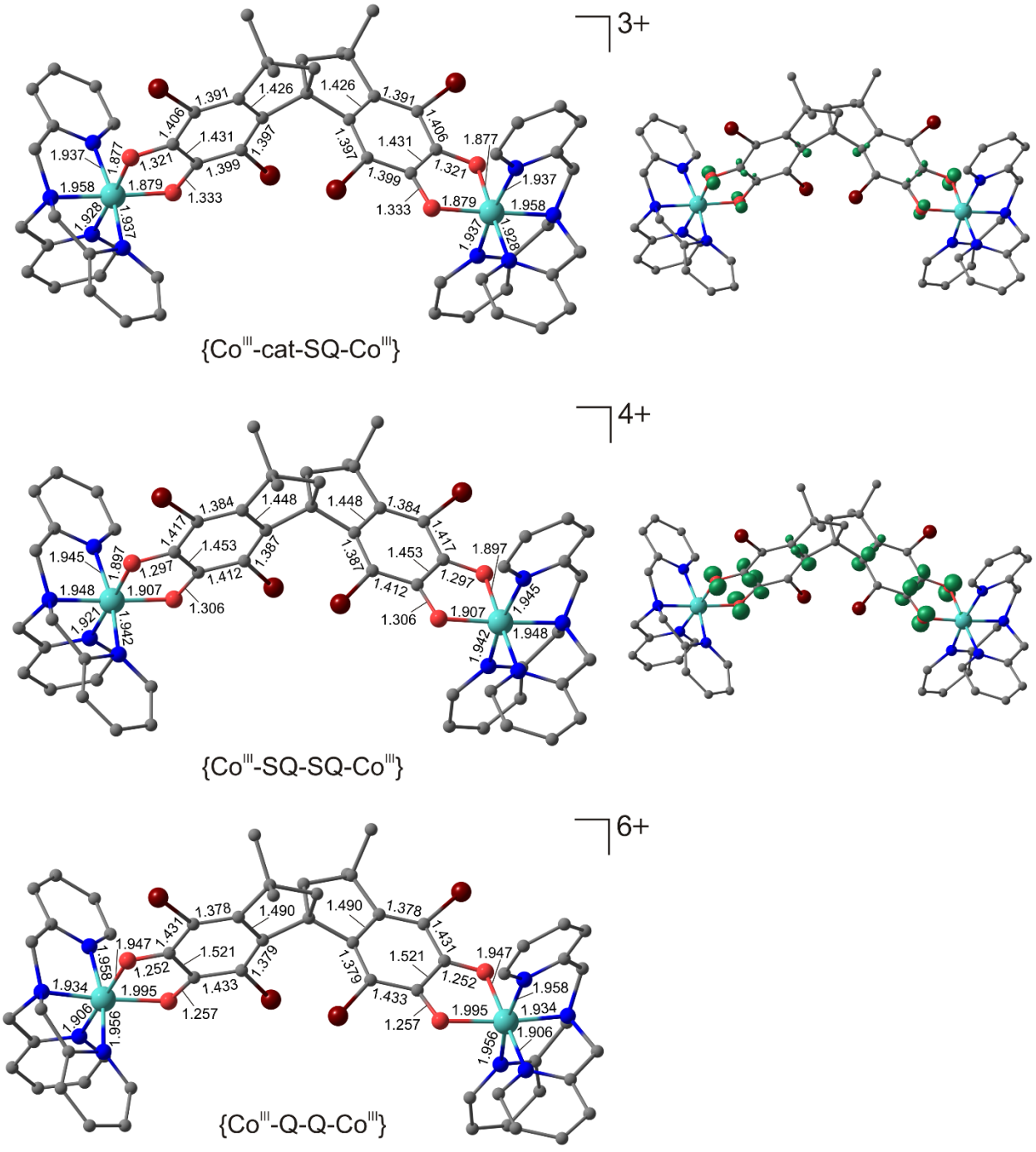

Figure S27. Optimized geometries (*left*) and spin density distribution (cutoff = 0.015 e/Å^3) (*right*) of the oxidized species of $\mathbf{2_{pp}}^{2+}$ as calculated by the DFT UTPSSh/6-311++G(d,p) method.

Analogous calculations performed on complex $\mathbf{4}^{2+}$ (Figure S28) indicate that processes **I** and **II** are sequential ligand-based one-electron reductions. A one-electron reduction of $\mathbf{4}^{2+}$ (process **I**) results in the formation of a $\{Co^{II}\text{-SQ-cat-}Co^{II}\}$ species, $\mathbf{4}^{+}$, with non-equivalent dioxolene moieties (Figure S29). The second one-electron reduction (process **II**) stabilizes the $\{Co^{II}\text{-cat-cat-}Co^{II}\}$ species, **4**, as indicated by typical catecholate bond lengths in the dioxolene fragments and localized spin density on the cobalt atoms (Figure S29). Removing two electrons from complex $\mathbf{4}^{2+}$ (process **III**) could result in two possible $\mathbf{4}^{4+}$ species, $\{Co^{III}\text{-SQ-SQ-}Co^{III}\}$ from a metal-based oxidation and $\{Co^{II}\text{-Q-Q-}Co^{II}\}$ from a ligand-based oxidation (Figure S28). The $\{Co^{II}\text{-Q-Q-}Co^{II}\}$ state is destabilized by 25 kcal mol^{-1} relative to the $\{Co^{III}\text{-SQ-SQ-}Co^{III}\}$ species. However, based on convincing experimental evidence that process **III** is ligand-based, we conclude that the kinetically favored process is an oxidation to the $\{Co^{II}\text{-Q-Q-}Co^{II}\}$ species which may be followed by a rearrangement to the more enthalpically stable $\{Co^{III}\text{-SQ-SQ-}Co^{III}\}$ species. The $\{Co^{III}\text{-SQ-SQ-}Co^{III}\}$ state is characterized by short Co-O/N bond lengths, absence of spin density on the cobalt atoms and localized spin density on the semiquinone fragments (Figure S28).

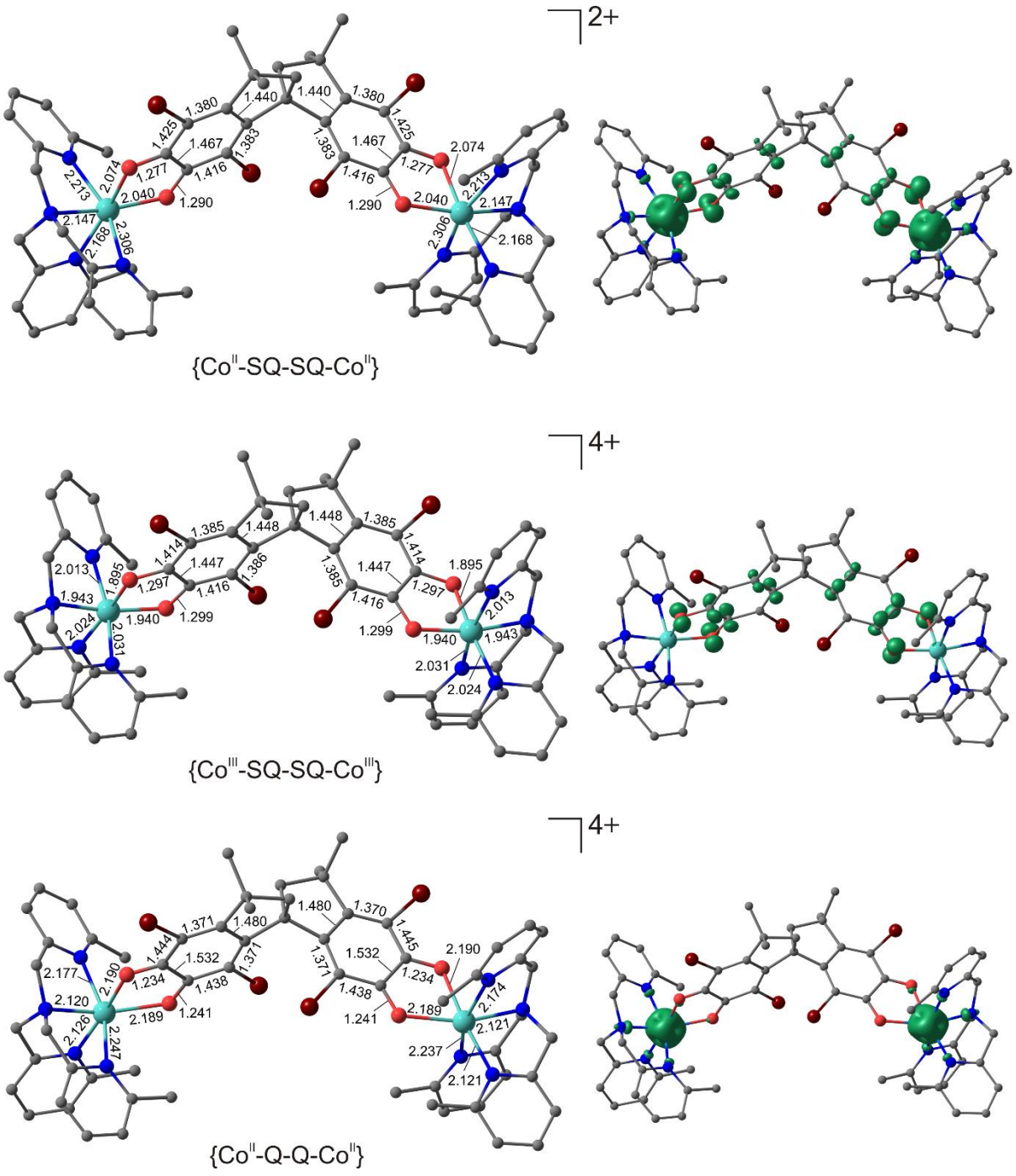

Figure S28. Optimized geometries (*left*) and spin density distribution (cutoff = 0.015 e/Å^3) (*right*) of the initial and oxidized species of **4**$^{2+}$ as calculated by the DFT UTPSSh/6-311++G(d,p) method.

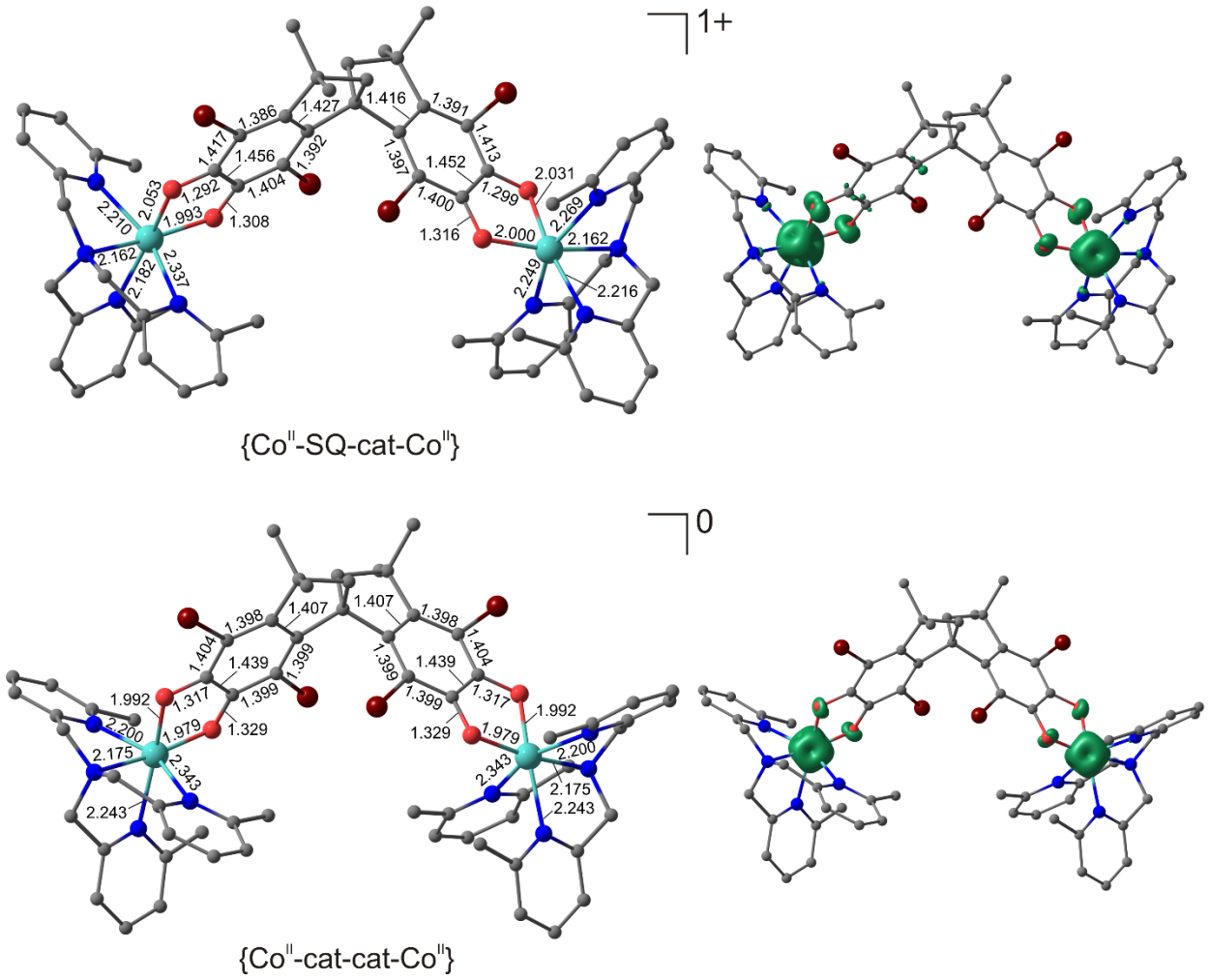

Figure S29. Optimized geometries (*left*) and spin density distribution (cutoff = 0.015 e/Å^3) (*right*) of the reduced species of $\mathbf{4}^{2+}$ as calculated by the DFT UTPSSh/6-311++G(d,p) method.

Computational Investigation of Magnetic Properties

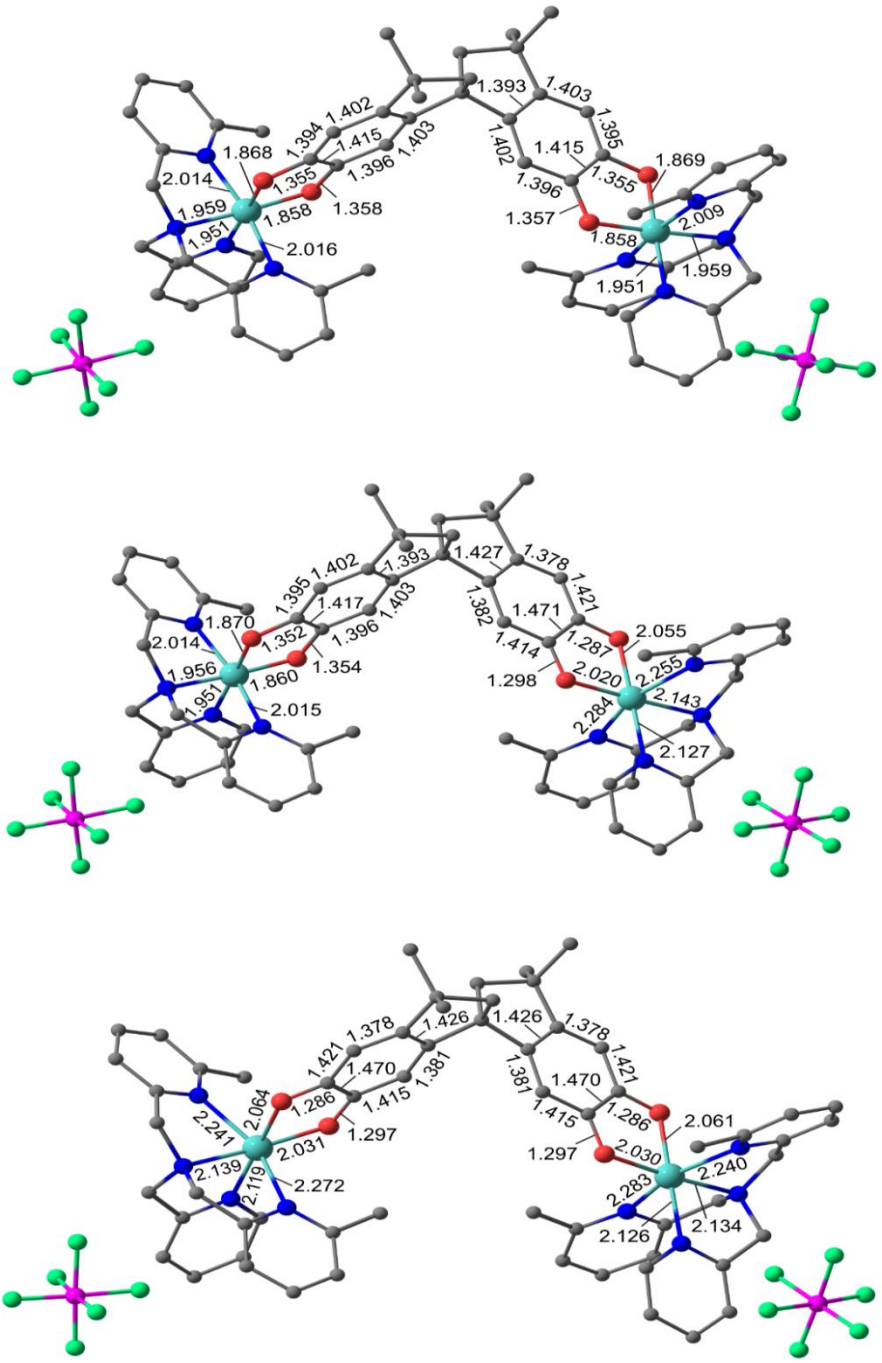

Figure S30. Optimized geometries of **1a** in the three charge distributions, {Co^{III}-cat-cat-Co^{III}} (top), {Co^{III}-cat-SQ-Co^{II}} (middle) and {Co^{II}-SQ-SQ-Co^{II}} (bottom) as calculated by the DFT UTPSSh/6-311++G(d,p) method.

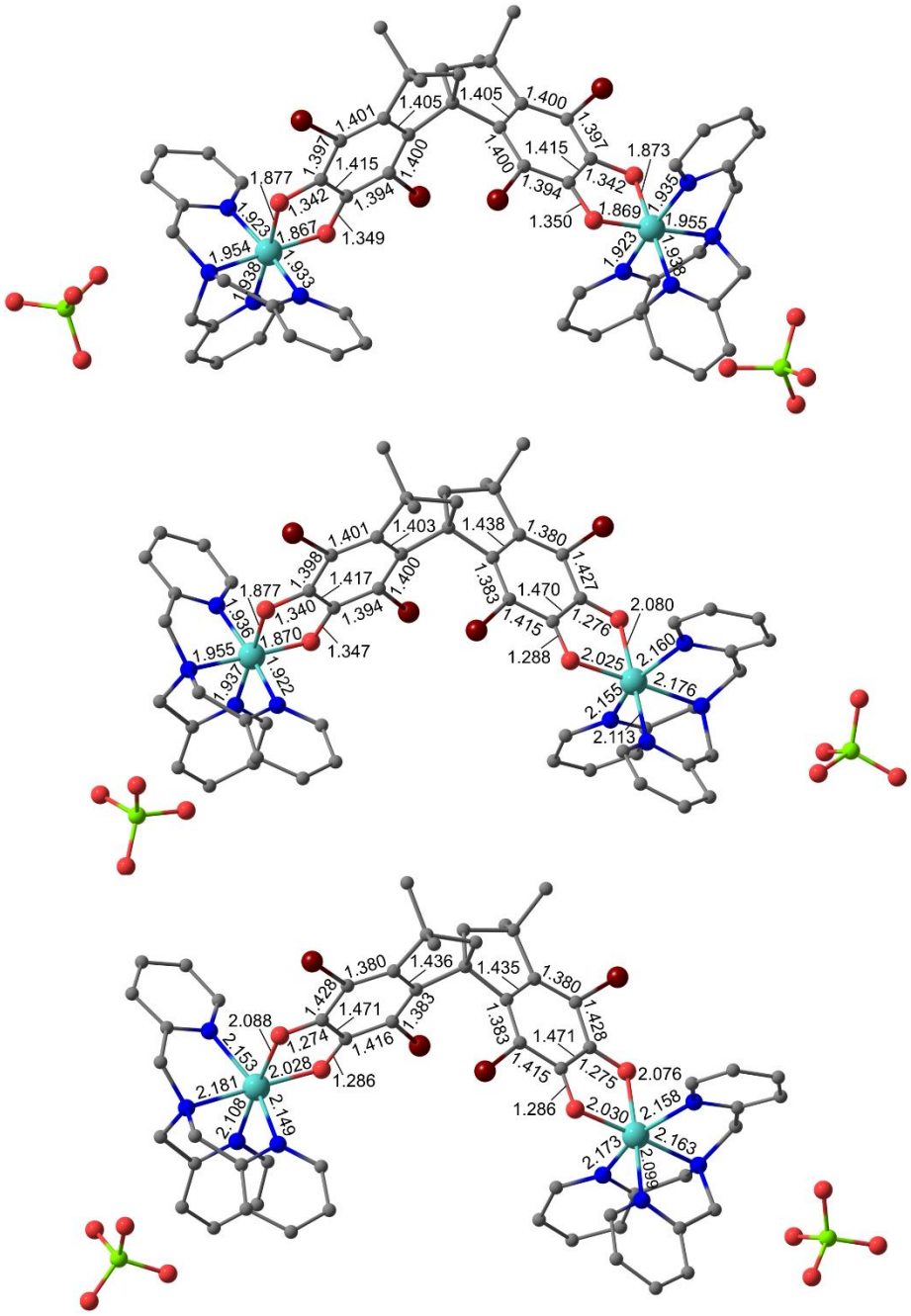

Figure S31. Optimized geometries of **2b$_{pp}$** in the three charge distributions, {Co^{III}-cat-cat-Co^{III}} (top), {Co^{III}-cat-SQ-Co^{II}} (middle) and {Co^{II}-SQ-SQ-Co^{II}} (bottom) as calculated by the DFT UTPSSh/6-311++G(d,p) method.

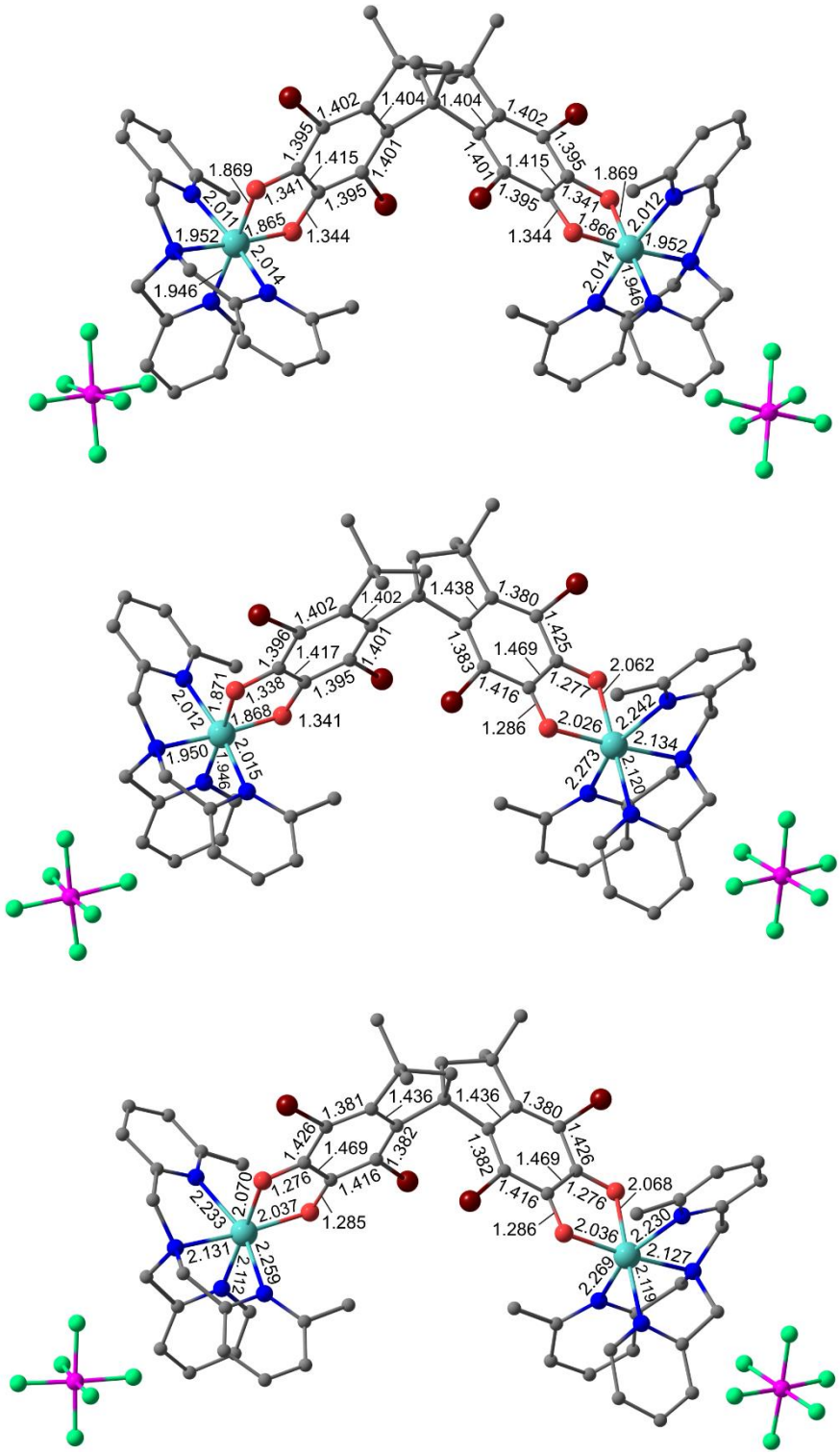

Figure S32. Optimized geometries of **3a** in the three charge distributions, {Co^{III}-cat-cat-Co^{III}} (top), {Co^{III}-cat-SQ-Co^{II}} (middle) and {Co^{II}-SQ-SQ-Co^{II}} (bottom) as calculated by the DFT UTPSSh/6-311++G(d,p) method.

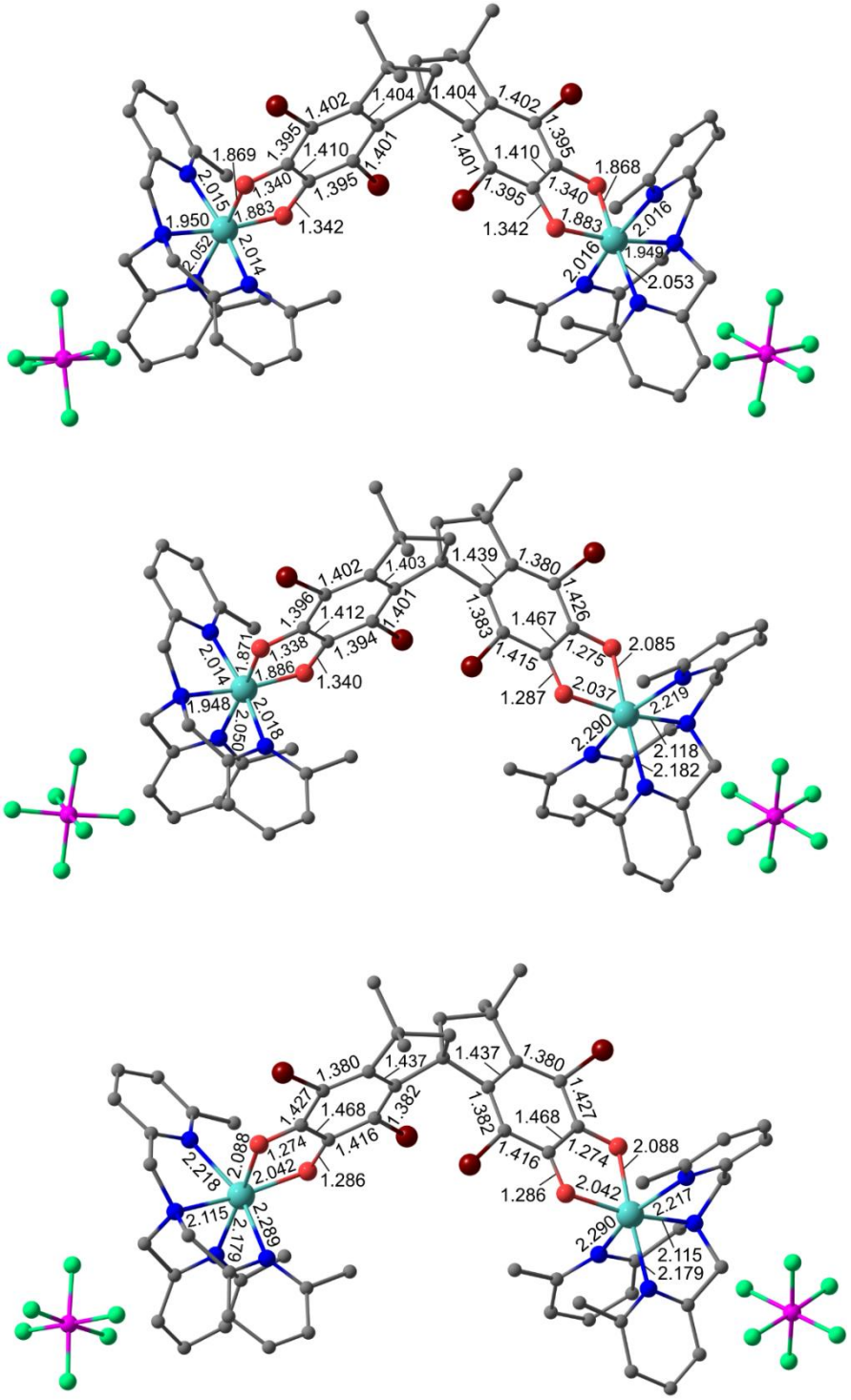

Figure S33. Optimized geometries of **4a** in the three charge distributions, {Co^{III}-cat-cat-Co^{III}} (top), {Co^{III}-cat-SQ-Co^{II}} (middle) and {Co^{II}-SQ-SQ-Co^{II}} (bottom) as calculated by the DFT UTPSSh/6-311++G(d,p) method.

Table S15. Spin states (S), total energies with (E^{ZPE}) and without (E) zero-point harmonic vibrations, total enthalpies (H^{298}) and expectation values of the spin-squared operator ($\hat{S}^2$) of the compounds **1a**, **2b$_{pp}$**, **2b$_{pd}$**, **3a** and **4a** calculated by the DFT UTPSSh/6-311++G(d,p) method.

	Charge Distribution	***S***	***E*/a.u.**	***E*^{ZPE}/a.u.**	***H*^{298}/a.u.**	***Ŝ*^{2}**
1a	{Co^{III}-cat-cat-Co^{III}}	0	–7750.275392	–7749.096719	–7749.011792	0.00
	{Co^{III}-cat-SQ-Co^{II}}	2	–7750.273710	–7749.098189	–7749.012002	6.01
	βα [a]	1	–7750.271258	–	–	3.00
	{Co^{II}-SQ-SQ-Co^{II}}	4	–7750.269035	–7749.097500	–7749.009197	20.03
	αββα	2	–7750.263269	–	–	7.95
	ααββ	0	–7750.269106	–	–	4.02
	αβαβ	0	–7750.263216	–	–	4.01
	αβαα	3	–7750.266295	–	–	13.01
	βααα	1	–7750.266252	–	–	5.02
2b$_{pp}$	{Co^{III}-cat-cat-Co^{III}}	0	–17526.842655	–17525.821090	–17525.741539	0.00
	{Co^{III}-cat-SQ-Co^{II}}	2	–17526.822977	–17525.805453	–17525.724027	6.01
	βα	1	–17526.820711	–	–	3.00
	{Co^{II}-SQ-SQ-Co^{II}}	4	–17526.799116	–17525.785527	–17525.703018	20.03
	αββα	2	–17526.795590	–	–	8.00
	ααββ	0	–17526.799175	–	–	4.02
	αβαβ	0	–17526.795618	–	–	3.99
	αβαα	3	–17526.798390	–	–	13.01
	βααα	1	–17526.798378	–	–	5.01
2b$_{pd}$	{Co^{III}-cat-cat-Co^{III}}	0	–17526.842995	–17525.821448	–17525.742059	0.00
3a	{Co^{III}-cat-cat-Co^{III}}	0	–18043.989761	–18042.850608	–18042.759795	0.00
	{Co^{III}-cat-SQ-Co^{II}}	2	–18043.981794	–18042.846607	–18042.753803	6.01
	βα	1	–18043.978241	–	–	2.94
	{Co^{II}-SQ-SQ-Co^{II}}	4	–18043.971672	–18042.840397	–18042.745722	20.03
	αββα	2	–18043.965866	–	–	8.02
	ααββ	0	–18043.971676	–	–	4.02
	αβαβ	0	–18043.965874	–	–	4.01

	αβαα	3	–18043.968782	–	–	13.02
	βααα	1	–18043.968777	–	–	5.02
4a	{Co^{III}-cat-cat-Co^{III}}	0	–18122.633953	–18121.439804	–18121.346549	0.00
	{Co^{III}-cat-SQ-Co^{II}}	2	–18122.634145	–18121.443888	–18121.347726	6.01
	βα	1	–18122.631547	–	–	3.01
	{Co^{II}-SQ-SQ-Co^{II}}	4	–18122.631368	–18121.445268	–18121.347957	20.03
	αββα	2	–18122.625931	–	–	8.02
	ααββ	0	–18122.631012	–	–	4.01
	αβαβ	0	–18122.625941	–	–	4.01
	αβαα	3	–18122.628770	–	–	13.02
	βααα	1	–18122.628655	–	–	5.02

[a] α corresponds to spin-up, β corresponds to spin-down; the order of the paramagnetic centers in {Co^{II}-SQ-SQ-Co^{II}}: (1) Co^{II} (2) SQ (3) SQ (4) Co^{II}

Table S16. Relative energies of different charge distributions (kcal mol^{-1}) of **1a**, **$2b_{pp}$**, **3a** and **4a** and ρ-parameter calculated by the DFT UTPSSh/6-311++G(d,p) method.

	Charge distribution	**1a**	**$2b_{pp}$**	**3a**	**4a**
Energy/kcal mol^{-1}	{Co^{III}-cat-cat-Co^{III}}	0.0	0.0	0.0	0.0
	{Co^{III}-cat-SQ-Co^{II}}	1.1	12.3	5.0	–0.1
	{Co^{II}-SQ-SQ-Co^{II}}	4.0	27.3	11.4	1.6
ρ		–0.24	–0.05	–0.06	–0.57

Table S17. Exchange coupling parameters (cm^{-1}) calculated by the DFT UTPSSh/6-311++G(d,p) method.

Charge Distribution	**Coupled moieties** [a]	**1a**	**2b$_{pp}$**	**3a**	**4a**
{Co^{III}-cat-SQ-Co^{II}}	HS-Co(II)-SQ1	179	165	254	190
{Co^{II}-SQ-SQ-Co^{II}}	HS-Co(II)-SQ1	212	129	121	192
	HS-Co(II)-SQ2	–2	–1	0	7
	SQ1-SQ2	–6	–6	–1	6
	HS-Co(II)-HS-Co(II)	0	0	0	4

[a] SQ1 represents the closest (coordinating) dioxolene and SQ2 represents the dioxolene on the other side of Br$_4$spiro.

References

1. Robinson, W. R., Perchlorate salts of metal ion complexes: Potential explosives. *J. Chem. Educ.* **1985,** *62*, 1001.
2. Fuentes, O.; Paudler, W. W., Synthesis of 2-azacycl[3.2.2]azine. *J. Org. Chem.* **1975,** *40*, 1210–1213.
3. Beni, A.; Dei, A.; Laschi, S.; Rizzitano, M.; Sorace, L., Tuning the charge distribution and photoswitchable properties of cobalt-dioxolene complexes by using molecular technique. *Chem. - Eur. J.* **2008,** *14*, 1804–1813.
4. Bravard, F. Complexation des cations lanthanides trivalents par des ligands azotés et oxygénés : études physico-chimiques de l'association et de la sélectivité en solution. Université Grenoble Alpes, 2004.
5. Molteni, V.; Rhodes, D.; Rubins, K.; Hansen, M.; Bushman, F. D.; Siegel, J. S., A new class of HIV-1 integrase inhibitors: The 3,3,3',3'-tetramethyl- 1,1'-spirobi(indan)-5,5',6,6'-tetrol family. *J. Med. Chem.* **2000,** *43*, 2031–2039.
6. Cowieson, N. P.; Aragao, D.; Clift, M.; Ericsson, D. J.; Gee, C.; Harrop, S. J.; Mudie, N.; Panjikar, S.; Price, J. R.; Riboldi-Tunnicliffe, A.; Williamson, R.; Caradoc-Davies, T., MX1: a bending-magnet crystallography beamline serving both chemical and macromolecular crystallography communities at the Australian Synchrotron. *J. Synchrotron Radiat.* **2015,** *22*, 187–190.
7. Aragao, D.; Aishima, J.; Cherukuvada, H.; Clarken, R.; Clift, M.; Cowieson, N. P.; Ericsson, D. J.; Gee, C. L.; Macedo, S.; Mudie, N.; Panjikar, S.; Price, J. R.; Riboldi-Tunnicliffe, A.; Rostan, R.; Williamson, R.; Caradoc-Davies, T. T., MX2: a high-flux undulator microfocus beamline serving both the chemical and macromolecular crystallography communities at the Australian Synchrotron. *J. Synchrotron Radiat.* **2018,** *25*, 885–891.
8. Rechkemmer, Y.; Fischer, J. E.; Marx, R.; Dörfel, M.; Neugebauer, P.; Horvath, S.; Gysler, M.; Brock-Nannestad, T.; Frey, W.; Reid, M. F.; van Slageren, J., Comprehensive Spectroscopic Determination of the Crystal Field Splitting in an Erbium Single-Ion Magnet. *J . Am. Chem. Soc.* **2015,** *137*, 13114–13120.
9. Kabsch, W., XDS. *Acta Cryst.* **2010,** *D66*, 125–132.
10. Sheldrick, G. M. *SADABS*, University of Göttingen, Germany, 1996.
11. Sheldrick, G. M., Crystal structure refinement with SHELXL. *Acta Cryst.* **2015,** *C71*, 3–8.
12. Sheldrick, G. M., SHELXT– Integrated space-group and crystal-structure determination. *Acta Cryst.* **2015,** *A71*, 3–8.
13. Dolomanov, O. V.; Bourhis, L. J.; Gildea, R. J.; Howard, J. A. K.; Puschmann, H., OLEX2: A complete structure solution, refinement and analysis program. *J. Appl. Cryst.* **2009,** *42*, 339–341.
14. Sheldrick, G., A short history of SHELX. *Acta Cryst.* **2008,** *A64*, 112–122.
15. Palatinus, L.; Chapuis, G., SUPERFLIP – a computer program for the solution of crystal structures by charge flipping in arbitrary dimensions. *J. Appl. Cryst.* **2007,** *40*, 786–790.
16. Spek, A. L., Single-crystal structure validation with the program PLATON. *J. Appl. Cryst.* **2003,** *36*, 7.
17. Spek, A. L. *PLATON, A Multipurpose Crystallographic Tool*, Utrecht, the Netherlands, 1998.
18. Le Page, Y., MISSYM1.1 – a flexible new release. *J. Appl. Cryst.* **1988,** *21*, 983–984.
19. de Souza, M. S.; Briganti, M.; Reis, S. G.; Stinghen, D.; Bortolot, C. S.; Cassaro, R. A. A.; Guedes, G. P.; da Silva, F. C.; Ferreira, V. F.; Novak, M. A.; Soriano, S.; Totti, F.; Vaz, M.

G. F., Magnetic Cationic Copper(II) Chains and a Mononuclear Cobalt(II) Complex Containing $[Ln(hfac)_4]^-$ Blocks as Counterions. *Inorg. Chem.* **2019,** *58*, 1976–1987.
20. *CrysAlisPro*, 1.171.39.46; Rigaku Oxford Diffraction: Yarnton, Oxfordshire, England, 2018.
21. Bain, G. A.; Berry, J. F., Diamagnetic Corrections and Pascal's Constants. *J. Chem. Educ.* **2008,** *85*, 532–536.
22. Frisch, M. J.; Trucks, G. W.; Schlegel, H. B.; Scuseria, G. E.; Robb, M. A.; Cheeseman, J. R.; Scalmani, G.; Barone, V.; Petersson, G. A.; Nakatsuji, H.; Li, X.; Caricato, M.; Marenich, A. V.; Bloino, J.; Janesko, B. G.; Gomperts, R.; Mennucci, B.; Hratchian, H. P.; Ortiz, J. V.; Izmaylov, A. F.; Sonnenberg, J. L.; Williams; Ding, F.; Lipparini, F.; Egidi, F.; Goings, J.; Peng, B.; Petrone, A.; Henderson, T.; Ranasinghe, D.; Zakrzewski, V. G.; Gao, J.; Rega, N.; Zheng, G.; Liang, W.; Hada, M.; Ehara, M.; Toyota, K.; Fukuda, R.; Hasegawa, J.; Ishida, M.; Nakajima, T.; Honda, Y.; Kitao, O.; Nakai, H.; Vreven, T.; Throssell, K.; Montgomery Jr., J. A.; Peralta, J. E.; Ogliaro, F.; Bearpark, M. J.; Heyd, J. J.; Brothers, E. N.; Kudin, K. N.; Staroverov, V. N.; Keith, T. A.; Kobayashi, R.; Normand, J.; Raghavachari, K.; Rendell, A. P.; Burant, J. C.; Iyengar, S. S.; Tomasi, J.; Cossi, M.; Millam, J. M.; Klene, M.; Adamo, C.; Cammi, R.; Ochterski, J. W.; Martin, R. L.; Morokuma, K.; Farkas, O.; Foresman, J. B.; Fox, D. J. *Gaussian 16 (Revision A.03)*, Gaussian Inc.: Wallingford, CT, 2016.
23. Tao, J.; Perdew, J. P.; Staroverov, V. N.; Scuseria, G. E., Climbing the Density Functional Ladder: Nonempirical Meta-Generalized Gradient Approximation Designed for Molecules and Solids. *Phys. Rev. Lett.* **2003,** *91*, 146401.
24. Staroverov, V. N.; Scuseria, G. E.; Tao, J.; Perdew, J. P., Comparative assessment of a new nonempirical density functional: Molecules and hydrogen-bonded complexes. *J. Chem. Phys.* **2003,** *119*, 12129–12137.
25. Tezgerevska, T.; Rousset, E.; Gable, R. W.; Jameson, G. N. L.; Sañudo, E. C.; Starikova, A. A.; Boskovic, C., Valence tautomerism versus spin crossover in pyridinophane-cobalt-dioxolene complexes: an experimental and computational study. *Dalton Trans.* **2019,** *48*, 11674–11689.
26. Minkin, V. I.; Starikov, A. G.; Starikova, A. A., Computational insight into magnetic behavior and properties of the transition metal complexes with redox-active ligands: a DFT approach. *Pure Appl. Chem.* **2018,** *90*, 811–824.
27. Sato, D.; Shiota, Y.; Juhász, G.; Yoshizawa, K., Theoretical Study of the Mechanism of Valence Tautomerism in Cobalt Complexes. *J. Phys. Chem. A* **2010,** *114*, 12928–12935.
28. Adams, D. M.; Noodleman, L.; Hendrickson, D. N., Density Functional Study of the Valence-Tautomeric Interconversion Low-Spin $[Co^{III}(SQ)(Cat)(phen)] \rightleftharpoons$ High-Spin $[Co^{II}(SQ)_2(phen)]$. *Inorg. Chem.* **1997,** *36*, 3966–3984.
29. Starikova, A. A.; Chegerev, M. G.; Starikov, A. G.; Minkin, V. I., A DFT computational study of the magnetic behaviour of cobalt dioxolene complexes of tetraazamacrocyclic ligands. *Comput. Theor. Chem.* **2018,** *1124*, 15–22.
30. Piskunov, A. V.; Pashanova, K. I.; Ershova, I. V.; Bogomyakov, A. S.; Smolyaninov, I. V.; Starikov, A. G.; Kubrin, S. P.; Fukin, G. K., Pentacoordinated chloro-bis-o-iminosemiquinonato Mn^{III} and Fe^{III} complexes. *J. Mol. Struct.* **2018,** *1165*, 51–61.
31. Bannwarth, A.; Schmidt, S. O.; Peters, G.; Sönnichsen, F. D.; Thimm, W.; Herges, R.; Tuczek, F., FeIII Spin-Crossover Complexes with Photoisomerizable Ligands: Experimental and Theoretical Studies on the Ligand-Driven Light-Induced Spin Change Effect. *Eur. J. Inorg. Chem.* **2012,** *2012*, 2776–2783.

32. Cirera, J.; Paesani, F., Theoretical Prediction of Spin-Crossover Temperatures in Ligand-Driven Light-Induced Spin Change Systems. *Inorg. Chem.* **2012,** *51*, 8194–8201.
33. Noodleman, L., Valence bond description of antiferromagnetic coupling in transition metal dimers. *J. Chem. Phys.* **1981,** *74*, 5737–5743.
34. Shoji, M.; Koizumi, K.; Kitagawa, Y.; Kawakami, T.; Yamanaka, S.; Okumura, M.; Yamaguchi, K., A general algorithm for calculation of Heisenberg exchange integrals J in multispin systems. *Chem. Phys. Lett.* **2006,** *432*, 343–347.
35. *Chemcraft: version 1.7*, 2013.
36. Poneti, G.; Mannini, M.; Cortigiani, B.; Poggini, L.; Sorace, L.; Otero, E.; Sainctavit, P.; Sessoli, R.; Dei, A., Magnetic and Spectroscopic Investigation of Thermally and Optically Driven Valence Tautomerism in Thioether-Bridged Dinuclear Cobalt-Dioxolene Complexes. *Inorg. Chem.* **2013,** *52*, 11798–11805.
37. Alley, K. G.; Poneti, G.; Aitken, J. B.; Hocking, R. K.; Moubaraki, B.; Murray, K. S.; Abrahams, B. F.; Harris, H. H.; Sorace, L.; Boskovic, C., A Two-Step Valence Tautomeric Transition in a Dinuclear Cobalt Complex. *Inorg. Chem.* **2012,** *51*, 3944–3946.
38. Alley, K. G.; Poneti, G.; Robinson, P. S. D.; Nafady, A.; Moubaraki, B.; Aitken, J. B.; Drew, S. C.; Ritchie, C.; Abrahams, B. F.; Hocking, R. K.; Murray, K. S.; Bond, A. M.; Harris, H. H.; Sorace, L.; Boskovic, C., Redox Activity and Two-Step Valence Tautomerism in a Family of Dinuclear Cobalt Complexes with a Spiroconjugated Bis(dioxolene) Ligand. *J. Am. Chem. Soc.* **2013,** *135*, 8304–8323.
39. Suenaga, Y.; Pierpont, C. G., Binuclear Complexes of Co(III) Containing Extended Conjugated Bis(Catecholate) Ligands. *Inorg. Chem.* **2005,** *44*, 6183–6191.
40. Tourón Touceda, P.; Mosquera Vázquez, S.; Lima, M.; Lapini, A.; Foggi, P.; Dei, A.; Righini, R., Transient infrared spectroscopy: a new approach to investigate valence tautomerism. *Phys. Chem. Chem. Phys.* **2012,** *14*, 1038–1047.
41. Alley, K. G. Towards Valence Tautomerism in Polynuclear Complexes, PhD Thesis. The University of Melbourne, Melbourne, VIC, 2012.
42. Rupp, F.; Chevalier, K.; Graf, M.; Schmitz, M.; Kelm, H.; Grün, A.; Zimmer, M.; Gerhards, M.; van Wüllen, C.; Krüger, H.-J.; Diller, R., Spectroscopic, Structural, and Kinetic Investigation of the Ultrafast Spin Crossover in an Unusual Cobalt(II) Semiquinonate Radical Complex. *Chem. - Eur. J.* **2017,** *23*, 2119–2132.
43. Xuan, X.; Wang, J.; Wang, H., Theoretical insights into PF6− and its alkali metal ion pairs: geometries and vibrational frequencies. *Electrochim. Acta* **2005,** *50*, 4196–4201.
44. Brown, S. N., Metrical Oxidation States of 2-Amidophenoxide and Catecholate Ligands: Structural Signatures of Metal-Ligand π Bonding in Potentially Noninnocent Ligands. *Inorg. Chem.* **2012,** *51*, 1251–1260.
45. Carugo, O.; Castellani, C. B.; Djinović, K.; Rizzi, M., Ligands derived from o-benzoquinone: statistical correlation between oxidation state and structural features. *J. Chem. Soc., Dalton Trans.* **1992**, 837–841.
46. Llunell, M.; Casanova, D.; Cirera, J.; Alemany, P.; Alvarez, S. *SHAPE*, 2.1; Universitat de Barcelona: Barecelona, Spain, 2013.
47. Alvarez, S.; Avnir, D.; Llunell, M.; Pinsky, M., Continuous symmetry maps and shape classification. The case of six-coordinated metal compounds. *New J. Chem.* **2002,** *26*, 996–1009.
48. Halcrow, M. A., Structure:function relationships in molecular spin-crossover complexes. *Chem. Soc. Rev.* **2011,** *40*, 4119–4142.

49. Ketkaew, R.; Tantirungrotechai, Y.; Harding, D. J.; Harding, P.; Marchivie, M. *OctaDist version 2.4*, 2019.
50. da Silva, A. F. M.; de Mello, M. V. P.; Gómez, J. G.; Ferreira, G. B.; Lanznaster, M., Investigation of cobalt(III)-tetrachlorocatechol complexes as models for catechol-based anticancer prodrugs. *Eur. J. Inorg. Chem.* **2019**, 1784–1791.
51. Benelli, C.; Dei, A.; Gatteschi, D.; Pardi, L., Redox potentials and charge transfer spectra of catecholate and semiquinone adducts of a cobalt-tetraazamacrocyclic complex. *Inorg. Chim. Acta* **1989,** *163*, 99–104.
52. Banci, L.; Bencini, A.; Benelli, C.; Gatteschi, D.; Zanchini, C., Spectral-structural correlations in high-spin cobalt(II) complexes. In *Structures versus Special Properties*, Springer Berlin Heidelberg: Berlin, Heidelberg, 1982; pp 37–86.
53. Bencini, A.; Beni, A.; Costantino, F.; Dei, A.; Gatteschi, D.; Sorace, L., The influence of ligand field effects on the magnetic exchange of high-spin Co(II)-semiquinonate complexes. *Dalton Trans.* **2006**, 722–729.
54. Dei, A.; Feis, A.; Poneti, G.; Sorace, L., Thermodynamics of valence tautomeric interconversion in a tetrachlorodioxolene:cobalt 1:1 adduct. *Inorg. Chim. Acta* **2008,** *361*, 3842–3846.
55. Loughrey, J. J.; Sproules, S.; McInnes, E. J. L.; Hardie, M. J.; Halcrow, M. A., Stable Mixed-Valent Radicals from Platinum(II) Complexes of a Bis(dioxolene) Ligand. *Chem. - Eur. J.* **2014,** *20*, 6272–6276.
56. Robin, M. B.; Day, P., Mixed valence chemistry. A survey and classification. *Advan. Inorg. Chem. Radiochem.* **1967,** *10*, 247–422.
57. Demadis, K. D.; Hartshorn, C. M.; Meyer, T. J., The Localized-to-Delocalized Transition in Mixed-Valence Chemistry. *Chem. Rev.* **2001,** *101*, 2655–2686.
58. D'Alessandro, D. M.; Keene, F. R., Current trends and future challenges in the experimental, theoretical and computational analysis of intervalence charge transfer (IVCT) transitions. *Chem. Soc. Rev.* **2006,** *35*, 424–440.
59. Arnold, A.; Sherbow, T. J.; Sayler, R. I.; Britt, R. D.; Thompson, E. J.; Muñoz, M. T.; Fettinger, J. C.; Berben, L. A., Organic Electron Delocalization Modulated by Ligand Charge States in $[L_2M]^{n-}$ Complexes of Group 13 Ions. *J. Am. Chem. Soc.* **2019,** *141*, 15792–15803.
60. Tahara, K.; Kadowaki, T.; Kikuchi, J.-i.; Ozawa, Y.; Yoshimoto, S.; Abe, M., Synthesis and Characterization of a New Series of Binuclear Pd(II) Biscatecholato Complexes: Non-Innocent Ligand-Based Approach to a Wide Range of Variation in Near-Infrared Absorptions of Mixed-Valence Complexes. *Bull. Chem. Soc. Jpn.* **2018,** *91*, 1630–1639.
61. Moneo, Á.; Justino, G. C.; Carvalho, M. F. N. N.; Oliveira, M. C.; Antunes, A. M. M.; Bléger, D.; Hecht, S.; Telo, J. P., Electronic Communication in Linear Oligo(azobenzene) Radical Anions. *J. Phys. Chem. A* **2013,** *117*, 14056–14064.
62. Meacham, A. P.; Druce, K. L.; Bell, Z. R.; Ward, M. D.; Keister, J. B.; Lever, A. B. P., Mono- and Dinuclear Ruthenium Carbonyl Complexes with Redox-Active Dioxolene Ligands: Electrochemical and Spectroscopic Studies and the Properties of the Mixed-Valence Complexes. *Inorg. Chem.* **2003,** *42*, 7887–7896.
63. Hush, N. S., Homogeneous and heterogeneous optical and thermal electron transfer. *Electrochim. Acta* **1968,** *13*, 1005–1023.
64. Allen, G. C.; Hush, N. S., Intervalence-Transfer Absorption. Part 2. Theoretical Considerations and Spectroscopic Data. In *Progress in Inorganic Chemistry*, Cotton, F. A., Ed. 1967; Vol. 7, pp 391–444.

65. Brunschwig, B. S.; Sutin, N., Energy surfaces, reorganization energies, and coupling elements in electron transfer. *Coord. Chem. Rev.* **1999,** *187*, 233–254.